Directional multipolelight transport model for rendering translucent materials

Diana Estefanía Naranjo Pomalaya

DISSERTATION PRESENTED
TO THE
INSTITUTO DE MATEMÁTICA E ESTATÍSTICA
OF THE
UNIVERSIDADE DE SÃO PAULO
FOR THE
OBTAINMENT OF THE TITLE
OF
MASTER IN SCIENCE

Program: Ciências da Computação

Adviser: Prof. Dr. Marcel Jackowski

Co-adviser: Prof. Dr. Nina Hirata

São Paulo, August – 2017

Directional multipole transport model for rendering translucent materials

This is the original version of the thesis developed by the candidate Diana Estefanía Naranjo Pomalaya, as is submitted to the judging committee.

Abstract

Translucent materials, such as milk or marble, are characterized by their soft and smooth appearance, as well as their bleed through effect when illuminated from behind. Diffusion based models are currently the best approximation of the real physical process that takes place underneath the surface of this kind of material. This process, dubbed subsurface scattering, is the one one responsible for the blurring effect that generates that soft appearance. The success of these models is due to the similarity between energy and light propagation. Since diffusion theory solves the problem of energy propagation, its use returns a good approximation of subsurface scattering. Aiming to produce a better approximation for translucent materials we developed an extension of a diffusion based subsurface scattering model called *directional multipole*. In our model we extend the directional dipole to achieve a better solution for thin slabs, i.e. shallow depths. The directional dipole is a model that uses a diffusion theory solution for a ray in an infinite medium, which comes closer to the representation of light rays since they have a magnitude and a direction. This is what differentiates it from the other diffusion based models, which are based on a solution for a point in an infinite medium. This model, however, fails to represent thin slabs because it assumes light steps are infinitely smaller than the depth of the object. Our model solves this problem by merging the directional dipole model with the multipole model, which was the first and only model that addresses this issue. By doing this, we created a model that achieves a closer approximation to the real for thin slabs than those of the multipole.

Keywords: Subsurface scattering, BSSRDF, light transport, diffusion theory, diffusion dipole, diffusion multipole, directional dipole

Contents

Chapter 1

Introduction

Physically-based rendering is an approach of computer graphics that aims to generate *photorealistic images*. This term means the goal is to make the generated images indistinguishable from real photographs. To achieve this, one may use models that emulate their real-world counterparts and the physical processes that takes place when an image is generated using a camera in the real world.

When an image is captured, what happens is that the light that originates from a source interacts with the objects until it reaches the camera. The final image is the result of the amount of light that arrived [PH10]. Light originates from sources such as lamps, smart-phone's screens and the sun; then, it propagates and interacts with all the objects within the scene. These interactions may change the path and the amount of light that will continue. These changes depend on the object's material properties. Finally, the image recorded is composed by the light that reaches the camera, which is equal to the amount that originated from a source, interacted with n objects in the scene and completed its path towards the camera.

(a) *Milk splash*   **(b)** *Marble statue of Cleopatra*
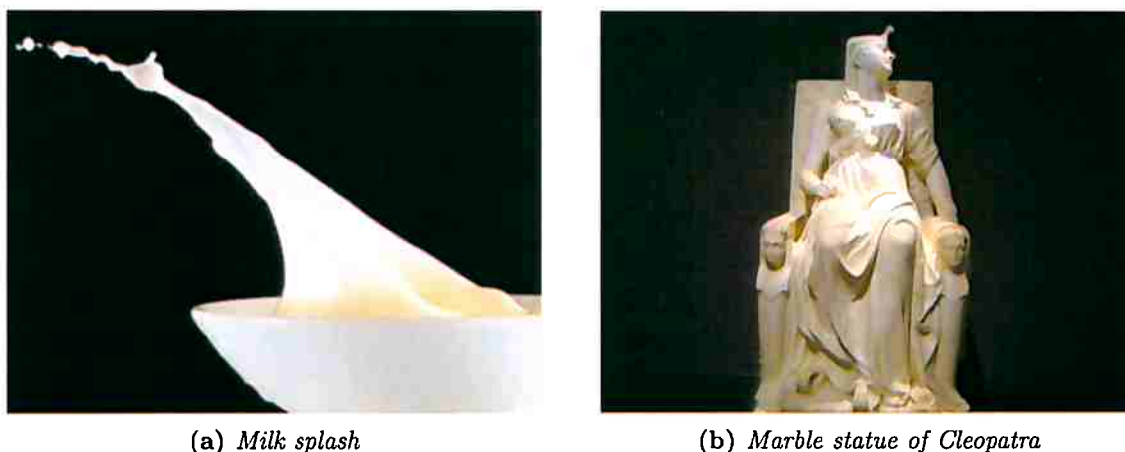
Figure 1.1: *Two translucent materials: (a) Milk splash [Pla08] and (b) a marble statue of Cleopatra [Rus06]*

In this project we will focus on the photo-realistic renderization of translucent materials, such as marble and milk. These kind of materials are characterized by their soft appearance and a sort of blur-effect on the small geometries of the surface, as shown in Figure 1.1. This figure depicts the photographs of a splash of milk and a marble statue of Cleopatra in the National Portrait Gallery (Washington, DC)[1]. Another important phenomenon of this kind of materials can be seen in Figure 1.1a, when thin objects with this composition are illuminated from behind: **light seems to bleed through**.

All these characteristics are produced by the light's path underneath the surface (*subsurface scattering*), as shown in Figure 1.2. Once light enters at some point x, it interacts with small

---

[1]Both of them were obtained from the Flickr website.

elements that compose the material [Ray71], and which affect light's path, before exiting at some other point y. These elements modify the amount of light that finally exits in different ways: some of the energy is lost, because light is absorbed, or its path is changed into a different direction (*out-scattering*); and some energy is gained because other paths change direction into the one being accounted for (*in-scattering*). If we were to simulate this process, we would need to track each light path; each change of direction or steps; and for each step we would need to check all other paths that might change direction into the one of interest. Because of all these possibilities, the computation becomes too expensive. Therefore, to generate an image that approximates objects with this kind of material a number of simplifications were generated.
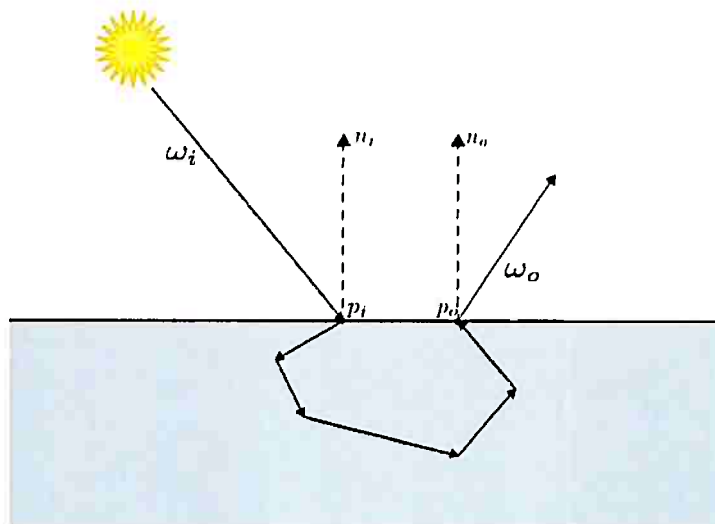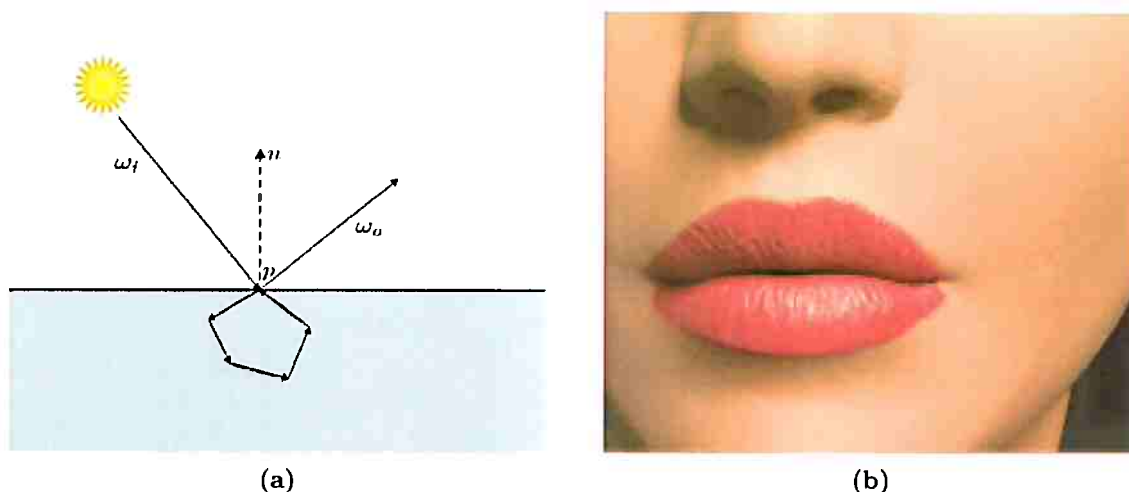

Figure 1.2: *Scattering of light in a BSSRDF model [INN07]*

The first simplification assumed that light exited at the same point it entered, as shown in Figure 1.3a. The function that represents this behaviour is called *Bidirectional Scattering Reflection Distribution*, and it offers a great approximation for materials like matte paint. However, its emulation of translucent materials is poor (Figure 1.3b). Therefore, new models arose and the most successful ones were based on the *diffusion theory*.

Diffusion theory was developed in order to solve the propagation of neutrons in a nuclear fusion reaction [GS55]. The solutions to these problem can also be employed to account for part of the amount of light that exists translucent materials, because of the duality between energy's and light's propagation. The portion that is computed by the diffusion theory solutions represent the light paths that have multiple interactions before exiting, called *multiple scattering*. We still have to compute the contribution of light that does not change direction, *reduced-radiance*, or changes it only once, known as *single scattering*. These last, however, can be computed without much computational cost. As a visual aid, multiple and single scattering can be seen in Figure 1.4. It is important to mention, as well, that the energy propagation has multiple solutions and therefore different approximations can be implemented.

One famous model that uses one of these diffusion theory solutions is known as *dipole diffusion* [JMLH01], developed by Jensen. This was the first model to present a function that relates the amount of light that exits at some point to the one that enters from all different directions in all the points of the surface. This function is known as *Bidirectional Surface Scattering Reflection Distribution Function*. As can be seen in Figure 1.5, especially in the area around the nose, the resulting skin simulation already has a softer look. Though this model achieves the soft appearance of translucent materials it fails to simulate the **bleed through of light** on **thin slabs**. This phenomenon occurs because a great part of the rays of light that enter the object from one face exist through the opposite one. The limitation to reproduce this behaviour is due to the dipole model's assumption that the object is semi-infinite. Working with this assumption means that a

Figure 1.3: *BRDF model: (a) Scattering of light in a BRDF [INN07] and (b) Face rendered with a BRDF model [INN07]*
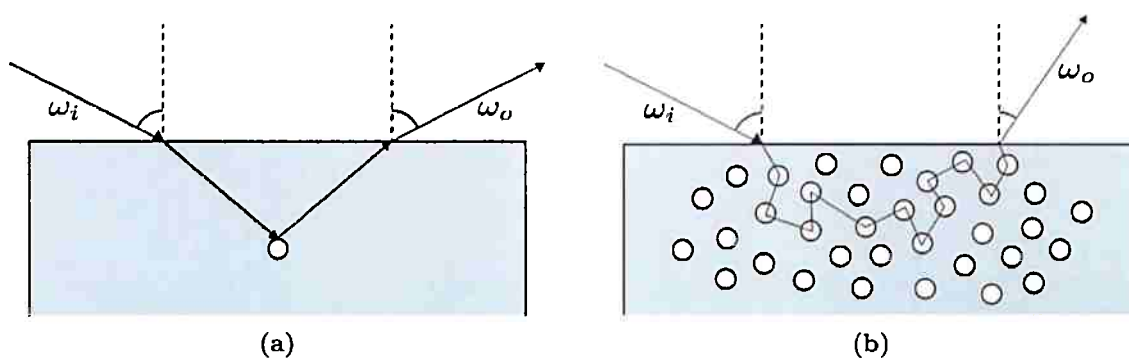
Figure 1.4: *Scattering paths segmentation: (a) Single scattering [RRBG06] and (b) Multiple scattering [RRBG06]*

good approximation will only occur when the object's depth is immensely bigger than the light's step within it. Since the light's step is directly proportional to the scattering properties of the material, this limitation varies between one material to the other. As an example, let's say this step is around $4mm$ in milk, any volume with a depth of approximately $8mm$ to $24mm$ will suffer a poor approximation. In order to surpass this limitation, a new model known as the *multipole* was developed by Donner and Jensen [DJ05].

Both of the previously described models were based on the same solution to the diffusion theory problem. This solution assumes that only one energy point-source exists in an infinite media. Manipulations of this solution made it possible to represent finite, and even thin, volumes. More recently, a new diffusion based model appeared, the *directional dipole*, proposed by Frisvad *et al.*. This model was based on a different solution to the diffusion theory problem: a solution for a ray [MSG05b] in an infinite medium. It introduced a BSSRDF which comes closer to path traced references because it takes into account the direction of incoming light, improving the accuracy of the analytic model [FHK14]. It, however, maintains the same semi-infinite limitation the dipole model suffered. We aimed to remove this limitation by extending the directional dipole solution for thin geometries. To achieve this, we developed a new model that produces a more accurate approximation of thin slabs based on the directional dipole and the multipole, dubbed *directional multipole*. We obtain a more accurate result in shallow depths because the new model takes this depth as a parameter of its calculations. It takes into consideration that part of the rays that hit the object might get transmitted through it and exit at the other surface.
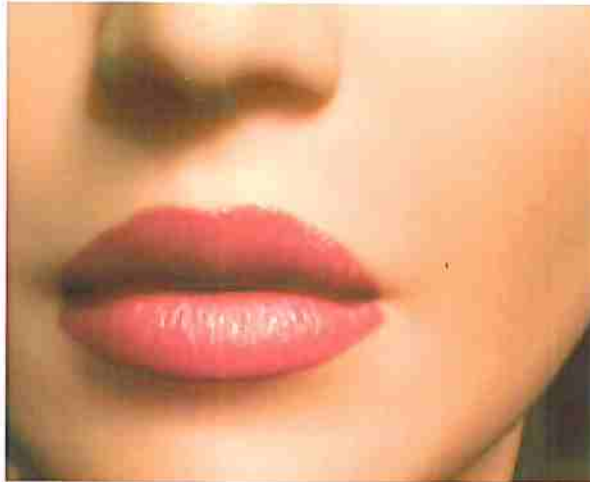
Figure 1.5: *Face rendered with a BSSRDF model [INN07]*

1.1   Objectives

- Create a new model for the realistic simulation of translucent materials in thin geometries, such as narrow slabs, by combining the *dirpole model*, which takes into consideration the direction of incident light; and the *multipole model*, which improves simulation of thin materials.

- Implement the new model in a rendering system which allows the visualization of the reflectance profile.

- Render a visualization of the reflectance profile of objects composed of shallow depths and translucent materials using this implementation.

- Compare numerical results obtained with other diffusion based models, such as the photon-beam, directional dipole and multipole.

- Compare the reflectance profile visualizations rendered using the new model with those rendered using other diffusion based models, such as the photon-beam, directional dipole and multipole.

1.2   Contributions

The main contributions of this work are:

- Comparison of current diffusion based models and evaluation of their advantages and limitations.

- Development of a new analytic shading model to accomplish realistic renderizations of thin slabs and translucent materials.

- Implementation of an algorithm that uses this new model to obtain a more accurate simulation of the reflectance profile given its thin geometry in the open-source renderer PBRT-v3.

1.3   Work organization

The remainder of this dissertation is organized as follows: Chapter 2 introduces the background concepts necessary to understand the proposed models. These concepts include the renderization process and the models used for the simulation of surface and volume scattering. Next, Chapter 3 introduces the concepts of diffusion theory as an approximation to solve the light transport problem

and the derivation of the standard dipole diffusion model. Followed by Chapter 4, which reviews the models based on diffusion approximation that succeeded the standard dipole model. The optimizations made by each one and their limitations are also included. Chapter 5 then presents an overview of the new model for translucent material renderization, based on the directional dipole and multipole models. This model generates accurate renderizations of shallow depths and translucent materials, evaluated in Chapter 6. Finally, Chapter 7 contains the conclusions of the tasks unfolded as well as ideas for future research.

Chapter 2

Background

To generate digital images, a process also known as rendering, based on the physical processes that happens in the real world, we need to use models that will represent those physical counterparts. As we previously mentioned, we need to determine the amount of light that reaches the camera from all points on the scene. This computation can be solved by the *rendering equation*. When dealing with translucent materials this equation gets a little more complicated and is known as the *volume rendering equation*. We will start by describing the process without any translucent materials, afterwards we will add them to finally obtain the complete process.

As an aid we have listed the most important symbols that we will use in Table 2.1.

2.1 Global illumination

When rendering an image our goal is to simulate all light interactions. We want to be able to calculate the amount of light that reaches the camera from any point in the scene. The algorithm responsible for this computation is called *global illumination*. To begin the description of this process we need to define the basic terminology of lightning.

2.1.1 Radiometry

The terminology used to describe light is called *radiometry*. The most basic quantity is called the *photon*, which determines the amount of energy in a specific wavelength[1]. The collection of photons is called radiant energy, Q, and is computed by integrating the energy of all the photons over all possible wavelengths. When we compute the time rate flow of radiant energy we get the *Flux*, $\Phi = \frac{dQ}{dt}$.

When we refer to the differential flux leaving a surface per differential area we are talking about *radiant emittance*, $M = \frac{d\Phi}{dA}$. Meanwhile, the *irradiance*, E refers to the differential flux arriving at a surface location.

Finally, *radiance*, L, is equal to the flux per unit solid angle per unit project area.

$$L = \frac{d^2\Phi}{d\omega dA^\perp},$$

where $dA^\perp$ is the projected area of dA on a hypothetical surface perpendicular to ω, as seen in Figure 2.1. The unit solid angle, $d\omega$, represents the direction of the ray and also a differential area of a unit sphere. They are the 3D analog of 2D angles.

Radiance is the concept that most closely represents the color of an object. It can be thought of as the number of photons arriving/leaving a small area per time. When it is arriving at the point we call it *incident radiance*; otherwise, we call it *exitant radiance*. Radiance describes the intensity of light at a given point in a given direction [Jen01]. We generally assume that radiance remains

---

[1]As we know, light has many wavelengths and humans are only able to distinguish those within the visible spectrum ($390 - 700nm$).

Symbol	Description
x	Position
x'	Position of incoming light
$\vec{n}$	Normal at x (always normalized: $|\vec{n}| = 1$)
$\vec{w}$	Direction (always away from surface)
$\vec{w}'$	Direction of incoming radiance (always away from surface)
$d\vec{w}$	Differential solid angle
$L(x, \vec{w})$	Radiance at x in direction $\vec{w}$
L_e	Emitted radiance
L_r	Reflected radiance
L_i	Incident radiance
Φ	Flux
E	Irradiance
f_s	Bidirectional Scattering Distribution Function
f_r	Bidirectional Reflectance Distribution Function
Ω	Hemisphere of directions
$\Omega_{4\pi}$	Sphere of directions
ρ	Phase function
η	Index of refraction
α	Albedo
σ_a	Absorption coefficient
σ_s	Scattering coefficient
σ_t	Extinction coefficient

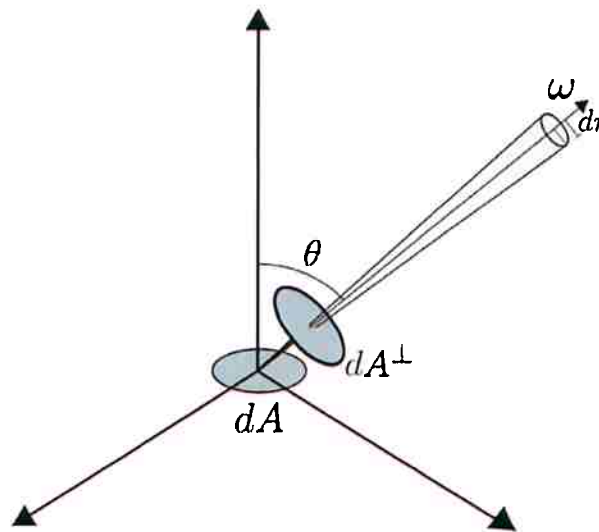**Table 2.1:** *Frequently used symbols [Jen01]*

Figure 2.1: *Radiance in a surface [PH10]*

unaltered during its path; however, this assumption offers a poor approximation in participating media, such as the one found within translucent materials.

2.1.2   Light sources

Light originates from light sources such as fire, the sun, or even a smart-phone's screen. The intensity of these light sources is described by their power, Φ_s. For example, given a differentially small sphere light source (point) that emits energy uniformly in all directions, we can compute the irradiance, E, that reaches a position x on a surface using Equation 2.1.

$$E(x) = \frac{\Phi_s \cos \theta}{4 \pi r^2},$$

(2.1)

where r is the distance from x to the light source and θ is the angle between the surface's

normal at position x and the direction to the light source. To explain this equation, imagine a sphere surrounding the source, as shown in Figure 2.2. The amount of power that will arrive at any point in the sphere (differential area surrounding it) will be $\Phi/(4\pi r^2)$. This is because all the power is being equally distributed onto the surface of the sphere. Meanwhile, the cosine term takes into consideration the surface's orientation. A surface that is directly facing the source will receive more photons per area that a surface oriented differently [Jen01]. The Lambert cosine law states that if the surface's normal $\vec{n}$ is tilted by an angle θ away from the light ray that arrives at that point, then the amount of energy deposited will be factored by $\cos\theta$ [Lam60].
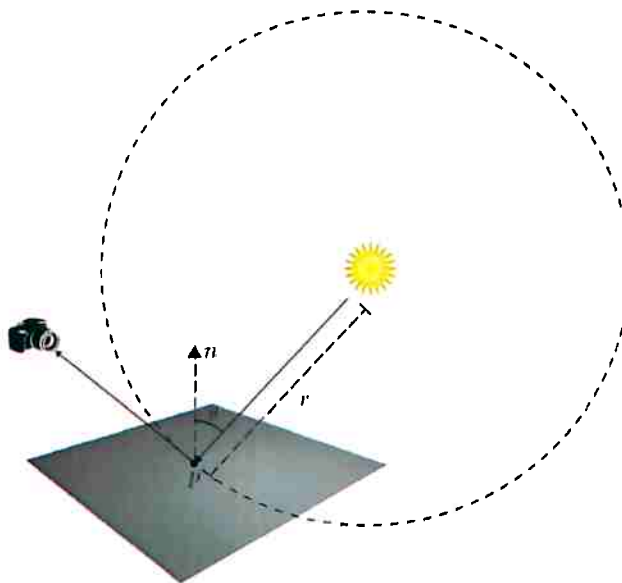

Figure 2.2: *Sphere centered at the light point source [PH10, Cli]*

2.1.3 Light scattering

As light travels trough the scene it might encounter some obstacle, such as a surface, a different medium or even a small particle (participating media). When this interaction takes place light may be scattered or absorbed.

BSSRDF

When a scattering event takes place between a surface and a ray of light, what really happens is that the ray enters the material, it scatters within and then exits at a different point on the surface. This process is presented in Figure 2.3. This behaviour is best appreciated in translucent materials, and is described by the *Bidirectional Scattering Surface Reflectance Distribution* or *BSSRDF*.

The BSSRDF, S, describes the ratio of differential exitant radiance, dL_r, at point x in direction $\vec{\omega}$ with respect to the differential incident flux $d\Phi_i$ at x' from direction $\vec{\omega'}$, where $\vec{\omega}$ and $\vec{\omega'}$ always point away from the surface. This relationship is described in Equation 2.2

$$S(x,\vec{\omega},x',\vec{\omega'}) = \frac{dL_r(x,\vec{\omega})}{d\Phi_i(x',\vec{\omega'})} \tag{2.2}$$

This is the most general description of light transport and is the only one that solves the subsurface scattering problem present in translucent materials. However, it is costly to evaluate since it has eight dimensions to take into account.
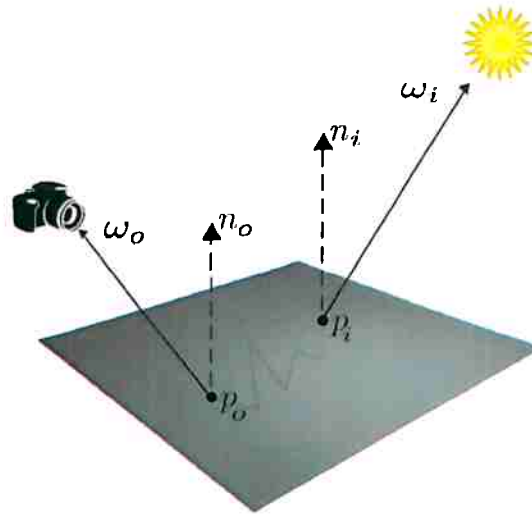
Figure 2.3: *BSSRDF model [PH10]*

BRDF

The *BRDF* or *Bidirectional Reflectance Distribution Function* is a simplification of the BSSRDF, it describes the reflection behavior on a surface at a single point. In Figure 2.4, we can see a visual relationship between the radiance leaving the surface, L_r, in the direction $\vec{\omega}$, as a result of incident radiance, L_i, from direction $\vec{\omega'}$.
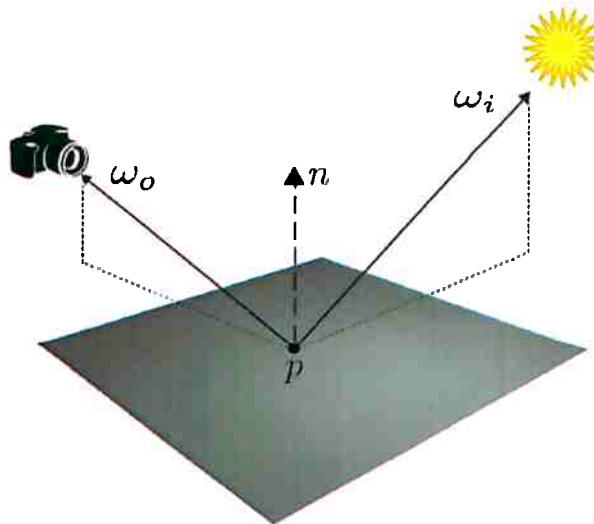

Figure 2.4: *BRDF model [PH10]*

The BRDF, f_r is defined as the proportionality between the differential exitant radiance and the differential irradiance $dE(x, \vec{\omega'})$. As shown in Equation 2.3.

$$f_r(x, \vec{\omega}, \vec{\omega'}) = \frac{dL_r(x, \vec{\omega})}{dE(x, \vec{\omega'})} = \frac{dL_r(x, \vec{\omega})}{L_i(x, \vec{\omega'})(\vec{n}\vec{\omega'})d\vec{\omega'}}, \tag{2.3}$$

where $\vec{n}$ is the normal at x.

To compute the reflected radiance at a point we need to integrate the incident radiance, as

shown in Equation 2.4.

$$L_r(x, \vec{\omega}) = \int_\Omega f_r(x, \vec{\omega}, vec\omega')L_i(x, \vec{\omega}')(\vec{n}\vec{\omega}')d\vec{\omega}', \tag{2.4}$$

where $(\vec{n}\vec{\omega}')$ is equal to $\cos\theta'$, and Ω is the hemisphere of incoming directions at x.

2.1.4   Rendering equation

The rendering equation is the mathematical description of global illumination. This equation describes the necessary conditions for equilibrium of light transport in scenes with no participating media. It can be used to compute the exitant radiance at any point in the model.

The exitant radiance is equivalent to the emitted radiance plus the reflected radiance:

$$L_o(x, \vec{\omega}) = L_e(x, \vec{\omega}) + L_r(x, \vec{\omega}),$$

by using Equation 2.4 to compute the reflected radiance we get Equation 2.5.

$$L_o(x, \vec{\omega}) = L_e(x, \vec{\omega}) + \int_\Omega f_r(x, \vec{\omega}, vec\omega')L_i(x, \vec{\omega}')(\vec{n}\vec{\omega}')d\vec{\omega}'. \tag{2.5}$$

2.2   Participating media

The rendering equation only works in models that do not have participating media. This is not the case when rendering a scene with translucent materials. After light rays enter a translucent material, the rays behave as in a participating medium. We will review the processes that occurs in this kind of environment.

2.2.1   Light scattering

When light enters a medium it can either continue its path unaltered or it can interact with the particles that compose it. When a photon interacts with the medium it is either scattered or absorbed. The parameters that determine which of these processes occur are the *scattering coefficient*, σ_s, and the *absorption coefficient*, σ_a. As a beam of light makes its path through the medium these interactions can be perceived as changes in the radiance of the ray [Jen01].

The change due to absorption interactions result in a reduction of radiance, as defined in Equation 2.6

$$(\vec{\omega} \cdot \nabla)L(x, \vec{\omega}) = -\sigma_a(x)L(x, \vec{\omega}). \tag{2.6}$$

The changes in light's direction due to the collision with particles result in *out-scattering* and *in-scattering*. The change due to out-scattering also results in the reduction in the radiance because some of the rays are deflected in different directions, as depicted in Figure 2.5 and defined in Equation 2.7.
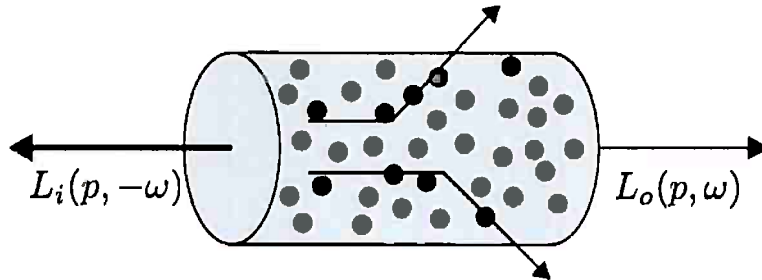

Figure 2.5: *Differential cylinder filled with out-scattering particles [PH10]*

$$(\vec{\omega} \cdot \nabla)L(x, \vec{\omega}) = -\sigma_s(x)L(x, \vec{\omega}). \tag{2.7}$$

When the reduction due to absorption and out-scattering are grouped together, we obtain the total reduction in radiance, defined in Equation 2.8

$$(\vec{\omega} \cdot \nabla)L(x,\vec{\omega}) = -\sigma_t(x)L(x,\vec{\omega}), \tag{2.8}$$

where $\sigma_t = \sigma_a + \sigma_s$.

As the ray moves through the media, the radiance of other rays that may be scattered into the ray's path, as depicted in Figure 2.6.
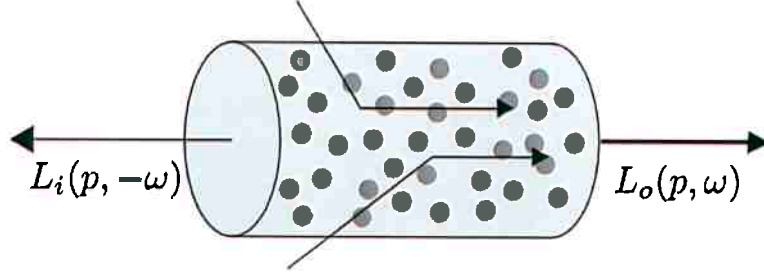

Figure 2.6: *Differential cylinder filled with in-scattering particles [PH10]*

The change in radiance due to in-scattering is defined by Equation 2.9

$$(\vec{\omega} \cdot \nabla)L(x,\vec{\omega}) = \sigma_s(x) \int_{\Omega_{4\pi}} \rho(x,\vec{\omega},\vec{\omega'})L_i(x,\vec{\omega'})d\vec{\omega'}, \tag{2.9}$$

which is the product of the scattering coefficient, σ_s, and the integral, over the sphere $\Omega_{4\pi}$ surrounding x, of the incident radiance and the phase function. The *phase function*, $\rho(x,\vec{\omega},\vec{\omega'})$, defines the probability distributions for scattering in a particular direction.

Finally, some participating media also presents an increment in radiance due to emission,

$$(\vec{\omega} \cdot \nabla)L(x,\vec{\omega}) = \sigma_a(x)L_e(x,\vec{\omega}).$$

Combining Equations 2.8 and 2.9 plus the changes due to emission, the total change in radiance per unit distance is Equation 2.10:

$$(\vec{\omega} \cdot \nabla)L(x,\vec{\omega}) = \sigma_a(x)L_e(x,\vec{\omega}) - \sigma_t(x)L(x,\vec{\omega}) + \sigma_s(x) \int_{\Omega_{4\pi}} \rho(x,\vec{\omega},\vec{\omega'})L_i(x,\vec{\omega'})d\vec{\omega'}. \tag{2.10}$$

2.2.2   Volume rendering equation

By integrating Equation 2.10 on both sides for a segment of length s, and adding incoming radiance from the other side of the medium we get Equation 2.11.

$$\begin{aligned}
L(x,\vec{\omega}) = &\int_0^s e^{-\tau(x,x')}\sigma_a(x')L_e(x',\vec{\omega'})dx' \\
&+ \int_0^s e^{-\tau(x,x')}\sigma_s(x') \int_{4\pi} p(x,\vec{\omega},\vec{\omega'})L_i(x',\vec{\omega'})d\vec{\omega'}dx' \\
&+ e^{-\tau(x,x+s\vec{\omega})}L(x - s\vec{\omega},\vec{\omega})
\end{aligned} \tag{2.11}$$

where $-\tau(x,x') = \int_x^{x'} \sigma_t(t)dt$ or $(x' - x)\sigma_t$ when the medium is homogeneous. This is known as the *volume rendering equation* and is more complex than the rendering equation. To accurately render translucent materials it is necessary to simulate this process within the object.

Chapter 3

Diffusion theory

The volume rendering equation accurately captures the subsurface scattering phenomenon that happens within translucent materials [DL76]. For the simulation of light transport, Harrahan and Krueger proposed a division of the scattering events into reduced-radiance, single and multiple scattering [HK93]. Reduced-radiance follows the original path of the light until it extinguishes; single scattering represents all the paths with only one scattering event within the medium before their exit; and, finally, multiple scattering represents all those with more than one scattering event before exiting.

Reduced-radiance and single scattering can be handled with simple approaches; multiple scattering, however, is almost as complicated as the original problem. To solve multiple scattering, Harrahan and Krueger proposed an algorithm that follows light paths recursively (*path tracing*) [HK93]. However, this algorithm can become really expensive. To improve upon this shortcoming, a different approach was proposed by Jensen [JMLH01], based on *diffusion approximation*. Diffusion theory aims to solve the propagation of energy. It was originally developed to solve the propagation of neutrons in a nuclear fusion reaction [GS55], but can also be used in the light propagation problem.

For the following sections, we will describe how the diffusion theory relates to the volume rendering equation and how the first model based on diffusion was created. To this end we have used Donner's thesis [Don06], Jensen's dipole model article [JMLH01] and PBRT's implementation of the same [PH10] as a basis.

3.1 Deriving the diffusion equation

We will start with the gradient version of the volume rendering equation, Equation 2.10, assuming that materials are homogeneous. Homogeneity means their scattering and absorption coefficients, as well as their phase function, will be constant throughout the medium. Renaming the emission term as Q, or *volumetric source* gives the Radiance Transfer Equation or RTE, Equation 3.1, for translucent materials.

$$(\vec{\omega} \cdot \nabla)L(x,\vec{\omega}) = -\sigma_t(x)L(x,\vec{\omega}) + \sigma_s(x)\int_{\Omega_{4\pi}} \rho(x,\vec{\omega},\vec{\omega}')L_i(x,\vec{\omega}')d\vec{\omega}' + Q(x,\vec{\omega}), \qquad (3.1)$$

The phase function ρ describes the anisotropic behavior of the material. Anisotropic materials present a varying appearance that changes according to the illumination direction, for example CDs are anisotropic, meanwhile a matte painted wall is isotropic because it looks the same regardless of the illumination setting. Since isotropic materials are much easier to model, the first simplification aims to reproduce the original anisotropic material as a new isotropic one.
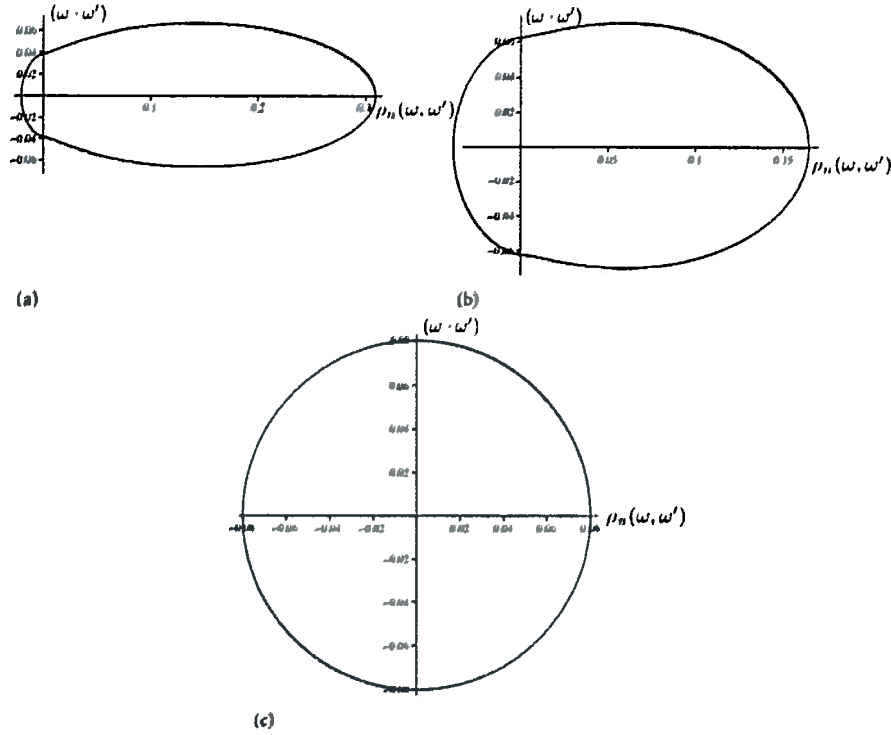
3.1.1 Principle of similarity

The *principle of similarity* states that anisotropic media with a high albedo, i.e. materials whose particles will reflect most incident illumination ($\sigma_s > \sigma_a$), can be approximated using isotropic

models with modified scattering and attenuation coefficients [PH10]. This approximation leads to a simplified solution thanks to the removal of anisotropy while maintaining a good relationship with the original model.

The principle of similarity derives from the observation that after a series of scattering events, the distribution of light in anisotropic, high albedo media, resembles a uniform directional distribution. This behavior can be appreciated in Figure 3.1, that shows the distribution of light that has been scattered 10, 100 and 1000 times respectively. This distribution is given by:

$$\rho_n(\vec{\omega}, \vec{\omega'}) = \frac{1 - g^{2n}}{4\pi(1 + g^{2n} - 2g|g^{n-1}|(-\vec{\omega} \cdot \vec{\omega'})^{3/2})},$$

where g is the anisotropy parameter, generated by computing the average cosine of the scattered direction. Its values vary between -1 and 1. As n grows large, this converges to the isotropic phase function, $1/4\pi$.

(a)   (b)

(c)

Figure 3.1: *Principle of similarity: (a) Directional distribution of a single incident ray of light after 10 scattering events in a highly anisotropic medium with the anisotropy parameter g equal to 0.9, (b) 100 scattering events, (c) 1000 scattering events [PH10]*

The new modified scattering and attenuation coefficients are called *reduced scattering coefficient*, σ'_s, and *reduced attenuation coefficient*, σ'_t. Their corresponding definitions are:

$$\sigma'_s = \sigma_s(1 - g),$$
$$\sigma'_t = \sigma_a + \sigma'_s.$$

The reduced coefficients are modified by the anisotropic parameter, which indicates the behaviour of the phase function. When $g = 0$ the phase function is constant and represents an isotropic scattering, when $g < 0$ the phase function is predominantly backward scattering, and correspondingly $g > 0$ indicates forward scattering dominance [JMLH01]. Translucent materials are mostly forward scattering with $g > 0.7$, e.g. skin $0.7 < g < 0.9$ [VGJSS89].

The anisotropic parameter helps the coefficients reach the isotropic behaviour. As an example,

consider a strongly forward scattering phase function with $g \to 1$. At every scattering event, the light is most likely to continue along the same path. In this situation, the value of σ'_s will be much smaller than the original σ_s, which means that there is less probability of a scattering event, leading to light traveling a larger distance in the medium before scattering [Don06].

3.1.2 Spherical harmonic expansion

Radiance is decomposed into *reduced-radiance*, L_{ri}, also known as *reduced intensity*, which accounts for the light rays that are parallel to each other, *single-scattering*, L_s, which accounts for rays that scatter once, and *multiple-scattering*, L_m, which accounts for those rays that scatter considerably and is, therefore, independent of direction. To solve multiple-scattering a truncated series of spherical harmonics is used to approximate the radiance [JMLH01]. Using the first four terms, we get a scalar ϕ and a vector terms $\mathbf{E}$, shown in Equation 3.2.

$$L_m(r,\vec{\omega}) \approx \frac{1}{4\pi}\phi(r) + \frac{3}{4\pi}\mathbf{E}(r)\cdot\omega \tag{3.2}$$

where r represents the distance between the incident point x' and the exitant one x, ϕ, called *fluence*, represents the average amount of light that enters a volume differential, it is related to *flux*, Φ; and $\mathbf{E}$, called *irradiance vector*, represents the current of light particles at a point in the medium, related to the *irradiance*, E, the scalar defined in Section 2.1. These parameters are defined as:

$$\Phi(r) = \int_{\Omega_{4\pi}} L_m(r,\vec{\omega})dvec\omega,$$

$$\mathbf{E}(r) = \int_{\Omega_{4\pi}} L_m(r,\vec{\omega})\vec{\omega}d\vec{\omega}.$$

3.1.3 Gradient substitution

When the spherical harmonics approximation is substituted in the Radiance Transfer Equation, Equation 3.1; and we perform an integration over all directions, $\vec{\omega}$ (details in [Ish78]), the result is Equation 3.3.

$$\nabla\phi(r) = -3\sigma'_t\mathbf{E}(r) + Q_1(r), \tag{3.3}$$

where $Q_1(r)$ is the 1st-order source term, $Q_1(r) = \int_{S^2} Q(r,\vec{\omega})\vec{\omega}d\vec{\omega}$, where Q is the source function (emission term). In the case of no sources, or when the sources are isotropic, Q_1 becomes zero, and, therefore, the irradiance vector equals the gradient of the fluence, as shown in Equation 3.4. This equation is known as *Fick's Law* [Fic55].

$$\mathbf{E}(r) = -\frac{1}{3\sigma'_t}\nabla\phi(r) = -D\nabla\phi(r), \tag{3.4}$$

where $D = \frac{1}{3\sigma'_t}$ is dubbed the *diffusion constant*.

3.1.4 The classic diffusion equation

Substituting Equation 3.4 into the Radiance Transfer Equation, Equation 3.1, and integrating over all directions $\vec{\omega}$ gives the **classic diffusion equation**, defined in Equation 3.5.

$$-D\nabla^2\phi(r) = \sigma_a\phi(r) - Q_0(r) + 3D\nabla\cdot Q_1(r), \tag{3.5}$$

where Q_0 represents the 0th-order source term, $Q_0(r) = \int_{S^2} Q(r,\omega)d\omega$.

3.1.5   BSSRDF and the radiant exitance

The reformulation of the general RTE to the local surface reflection integral gives the subsurface scattering equation.

$$L(x, \vec{\omega}) = \int_A \int_\Omega S(x, \vec{\omega}, x', \vec{\omega}') L_i(x', \vec{\omega}')(\vec{n}, \vec{\omega}') d\vec{\omega}' dA$$

A BSSRDF accounting only for multiple-scattering is termed S_d, which is simplified as a product of a diffuse reflectance profile R_d and a directional Fresnel term [JMLH01, dI11].

$$S_d(x, \vec{\omega}, x', \vec{\omega}') = \frac{1}{\pi} F_t(x', \vec{\omega}', \eta) R_d(|x - x'|) \frac{F_t(x, \vec{\omega}, \eta)}{4 C_\phi(1/\eta)} \tag{3.6}$$

where F_t represents the Fresnel transmittance that affects light at the entry and exit point, $4C_\phi$ is a constant needed for normalization, and η is the relative index of refraction[1]. R_d is equal to the radiant exitance divided by the incident flux:

$$R_d(r) = d\mathbf{E}(r) \cdot \vec{n}/d\Phi. \tag{3.7}$$

3.2   The dipole diffusion model

From the classic diffusion equation we proceed to explain how we can use the solutions to the diffusion equation to obtain a functional BSSRDF.

3.2.1   Diffusion equation solution

The diffusion equation, Equation 3.5, has a simple solution for a single point light source in an infinite medium [GS55]. The medium is assumed to be highly scattering and isotropic, which means no Q_1 term will be present, resulting in Equation 3.8:

$$\phi(r) = \frac{\Phi}{4\pi D} \frac{e^{-\sigma_{tr} r}}{r}, \tag{3.8}$$

known as *Green's function*, where $\sigma_{tr} = \sqrt{3\sigma_t' \sigma_a}$ is dubbed the *effective transport coefficient*.

3.2.2   Boundary Condition

Since Equation 3.8 is a solution for an infinite setting, it needs to be modified for a finite volume. To this end, a semi-infinite setting is adopted, where the $z = 0$ plane is located at the material's surface and the positive z axis, $\hat{z}$, points into the medium, opposite to the surface's normal, $\vec{n} = -\hat{z}$. This arrangement is depicted in Figure 3.2.

The diffusion equation needs to be solved subject to a *boundary condition* to achieve this setting. When the two interacting layers do not share the same index of refraction, light is internally reflected at the surface. The boundary condition in this case is defined such that the diffuse incident radiance reflected down at the surface in the $\vec{n}$ direction must be equal to the diffuse radiance in the $-\vec{n}$ axis [GFTB83]. This is depicted in Equation 3.9.

$$\int_{\Omega^+} L_d(r, \vec{\omega})(\vec{\omega} \cdot \vec{n}) d\vec{\omega} = \int_{\Omega^-} F_{dr} L_d(r, \vec{\omega})(\vec{\omega} \cdot -\vec{n}) d\vec{\omega} \qquad \text{at } z = 0, \tag{3.9}$$

where F_{dr} is the average *diffuse Fresnel reflectance*, which describes the amount of light reflected from a surface. This term is generally approximated with a simple polynomial expansion [GFTB83,

---

[1]The index of refraction describes how light propagates within a medium
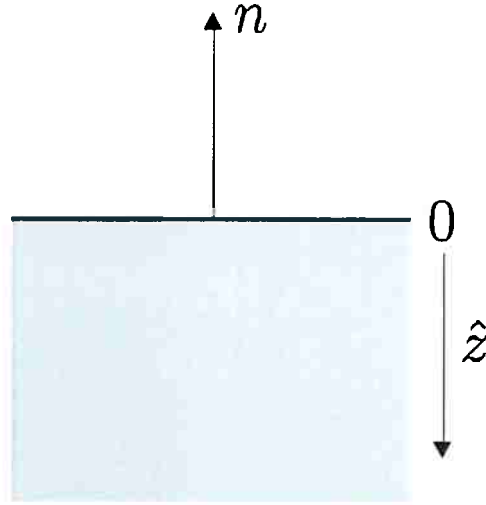
Figure 3.2: *Semi-infinite configuration with the positive z axis in the opposite direction to the surface's normal*

Rei73].

$$
F_{dr} \simeq \left\{ \begin{array}{l} -0.4399 + \frac{0.7099}{\eta} - \frac{0.3319}{\eta^2} + \frac{0.0636}{\eta^3}, \quad \eta < 1 \\ -\frac{1.4399}{\eta^2} + \frac{0.7099}{\eta} + 0.6681 + 0.0636\eta, \quad \eta > 1 \end{array} \right\},
\tag{3.10}
$$

where η is the relative index of refraction, i.e. the ratio between the two indices of refraction.

Using the spherical harmonics approximation, Equation 3.2, in Equation 3.9 gives the *outward flux*:

$$
\phi_0 + 2AD\frac{d\phi(r)}{dz} = 0
\tag{3.11}
$$

where ϕ_0 is the flux at the boundary and the A term is responsible for taking into account the effects of internal diffuse reflection and is defined as:

$$
A = \frac{1 + F_{dr}}{1 - F_{dr}}.
\tag{3.12}
$$

Assuming that the flux decreases linearly outside the diffusing material, then the gradient of the function is $d\phi(r)/dz = -\phi_0/(2AD)$. This assumption leads to flux vanishing at a distance $2AD$ beyond the boundary [GS55, FPB92]. Thus, the approximated surface boundary condition is: $\phi(2AD) = 0$. This distance above the surface is often called the extrapolated boundary [GS55].

3.2.3   Final BSSRDF

Equation 3.11 establishes that fluence goes to zero at a distance $2AD$ above the surface; which mirrors the falloff of fluence inside the medium as the boundary is approached. This boundary condition can be satisfied employing the *method of images*, which consists of a positive real source and a negative virtual source mirrored about the extrapolated boundary.

According to the assumptions so far established, the medium where the propagation takes place is a semi-infinite, highly isotropically scattering material. As light propagates through the material, the beam has a reduced intensity $L_{ri}(x) = L_i e^{-\sigma'_t x}$. This beam can be represented as an infinite set of point sources with decaying intensity. The average intensity scattered out of the beam is:

$$
\int_0^\infty \sigma'_s L_i e^{-\sigma'_t x} dx = \alpha' L_i,
$$

where $\alpha' = \sigma'_s/\sigma'_t$ is known as *reduced albedo*.

To simulate an incident ray of illumination, a point source is placed at a representative depth.

The distance light travels before interacting with a particle is described by the PDF $\sigma'_t e^{-\sigma'_t x}$. The average distance light travels is the expected value of this PDF:

$$\int_0^\infty x\sigma'_t e^{-\sigma'_t x}dx = \frac{1}{\sigma'_t},$$

known as mean-free-path (MFP) [PSW89, FPB92]. The point source is then placed at 1 MFP beneath the surface with its intensity equal to $\alpha' L_i$.

To satisfy the boundary condition, a virtual source is placed above the real source mirrored about the extrapolated boundary. Its height is $z_v = z_r + 4AD$ above the surface, as depicted in Figure 3.3. The resulting fluence is equal to the sum of the individual contributions from the two sources:

$$\phi(r) = \frac{\alpha'\Phi}{4\pi D}\left(\frac{e^{\sigma_{tr}d_r}}{d_r} - \frac{e^{\sigma_{tr}d_v}}{d_v}\right), \tag{3.13}$$

where $d_r = \sqrt{(r^2 + z_r^2)}$ and $d_v = \sqrt{(r^2 + z_v^2)}$ are the distances from p_i to the real and mirrored source respectively, as seen in Figure 3.3.
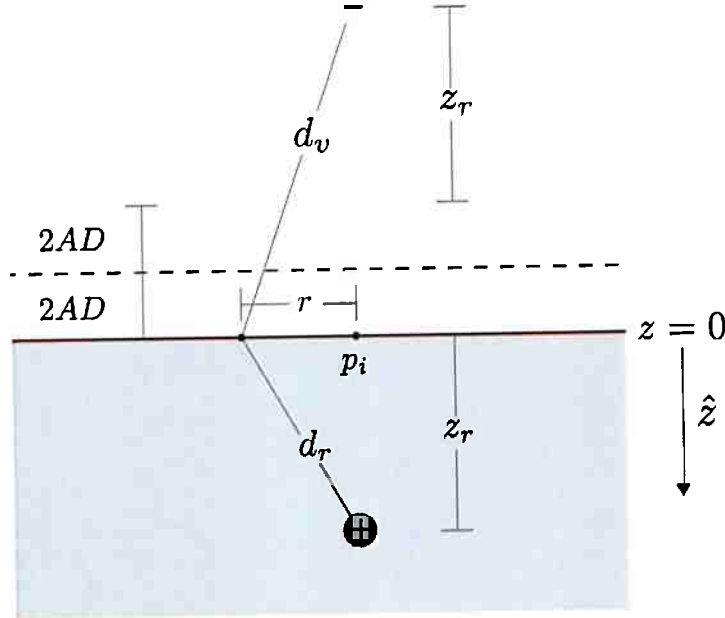
Figure 3.3: *Real and virtual source lights, representing an incident ray of light [Don06]*

Finally, these definitions allow the computation of the diffuse BSSRDF, S_d, dependent of the diffuse reflectance profile R_d, as stated in Equation 3.6. Since $R_d(r) = d(\mathbf{E}(r)\cdot n)/d\Phi$, according to Equation 3.7 and $\mathbf{E}(r) = -D\nabla\phi(r)$ following Fick's Law, Equation 3.4, we have:

$$R_d(r) = -D\frac{(n\cdot\nabla\phi)(r)}{d\Phi} \tag{3.14}$$

where $r = |x - x'|$.

Using the solution for fluence due to the dipole configuration, Equation 3.13, gives:

$$R_d(r) = \frac{\alpha'}{4\pi}\left[\frac{z_r(1 + \sigma_{tr}d_r)e^{-\sigma_{tr}d_r}}{d_r^3} + \frac{z_v(1 + \sigma_{tr}d_v)e^{-\sigma_{tr}d_v}}{d_v^3}\right]. \tag{3.15}$$

A more graphical representation of the diffuse reflectance profile is depicted in Figure 3.4. In this plot, we see the values of $R_d(r)$ for a range of r.
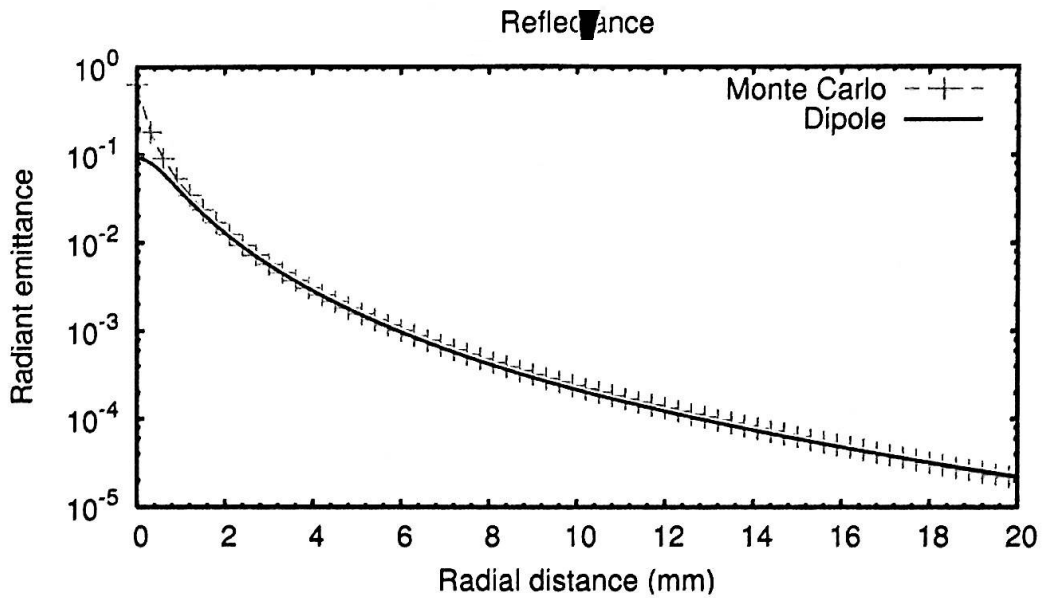
Figure 3.4: *Diffusion profile [Don06]*

3.2.4   Limitations

The dipole model is well suited for the approximation of optically thick, highly scattering, homogeneous materials [Don06]. The problem originates from the semi-infinite assumption. In the case of thin slabs [2], light may exit at the bottom (transmittance) instead of scattering back to the top surface. The dipole model is unable to simulate this situation.

It is also important to note that inaccuracies increase when the albedo decreases, as depicted in Figure 3.4. This error increases because light does not scatter very far from the incident point.
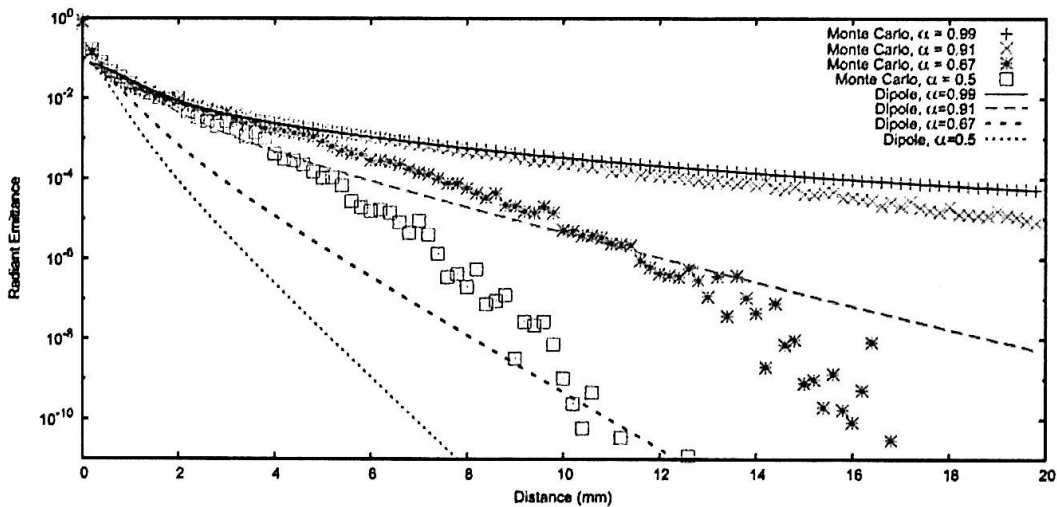
Figure 3.5: *Diffusion profiles compared with MC packet tracing for different albedo values [Don06]*

---

[2]Thickness of only a few MFP, $1MFP \approx 1mm$

Chapter 4

Evolution of the diffusion based models

4.1 Introduction

Since the development of the standard diffusion model in 2001 [JMLH01], a series of new diffusion-based approximations were presented in the search for optimization and expansion of the limits held so far. Figure 4.1 shows a timeline with the publication dates of some of these models. We have chosen to display only these because they made significant modifications to the BSSRDF model, not just optimizations in the implementation.
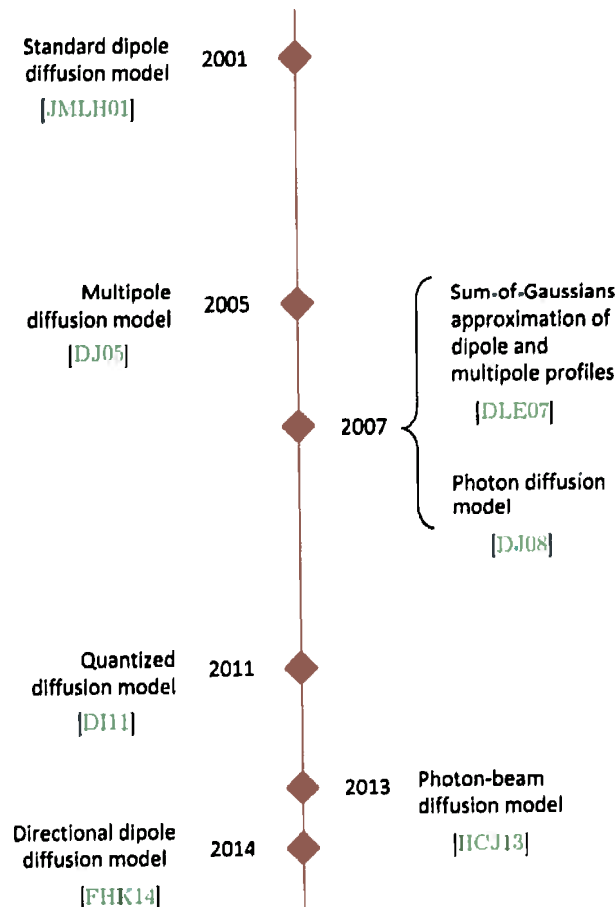
Figure 4.1: *Diffusion approximation models for translucent material renderization timeline*

The multipole diffusion approximation, developed by Donner and Jensen in 2005 [DJ05] enabled

21

the correct renderization of thin slabs and layered materials. When rendering slim volumes, the dipole model produced an overestimation of the reflected amount of light, because part of it is actually transmitted through the slab.

Later on, in 2007, Donner and Jensen developed the photon diffusion model [DJ08] aiming to cover more geometrically complex volumes and effects such as caustics, among others. Photon diffusion used photon tracing to calculate the diffusion of the photons' first interaction (scatter event) with the medium.

In 2011, d'Eon and Irving presented the quantized-diffusion model [dI11]. Their goal was to obtain a more realistic simulation of light's propagation. For this, they used the extended source, which computes the multiple scattering events for a beam as it passes through the medium, this leads to a model with multiple positive real sources. It, however, did not have an analytical solution and, therefore, a sum-of-Gaussians approximation was employed. Even though this approach provides a more accurate result, the methods used are complex, prone to errors, and require a considerable amount of storage. Aiming to solve these problems, the photon-beam diffusion model was developed by Habel et al. [HCJ13] in 2013. This model uses the Monte Carlo (MC) techniques instead of the sum-of-Gaussians approximation. By doing this, they reduced the computational complexity of the previous model.

Finally, in 2014, Frisvad et al. developed the direction dipole model [FHK14], also known as dirpole. This model is based on the solution of the diffusion equation for a ray of light in an infinite medium [MSG05b], meaning they already take into account the extended source in the diffusion equation solution so only one positive source is required. Its main limitation, however, is the same as that of the standard dipole model: it lacks support for geometrically complex volumes such as thin slabs.

In the following sections we will detail the models that served as basis for our new directional multipole model. These are the multipole model and the directional dipole. For our implementation we also used photon tracing, but we will leave these details for the next chapter.

4.2   The multipole diffusion model

The multipole model removes the semi-infinite restriction by extending the dipole model using multiple dipoles to account for thin geometries.

4.2.1   New boundary condition

The dipole approximation assumes that any light ray entering the material will be absorbed or returned to the surface (after some scattering events). In the case of thin slabs, light rays might get transmitted through them. This phenomenon reduces the amount of light diffusing back to the surface, which is why the dipole overestimates the reflectance.
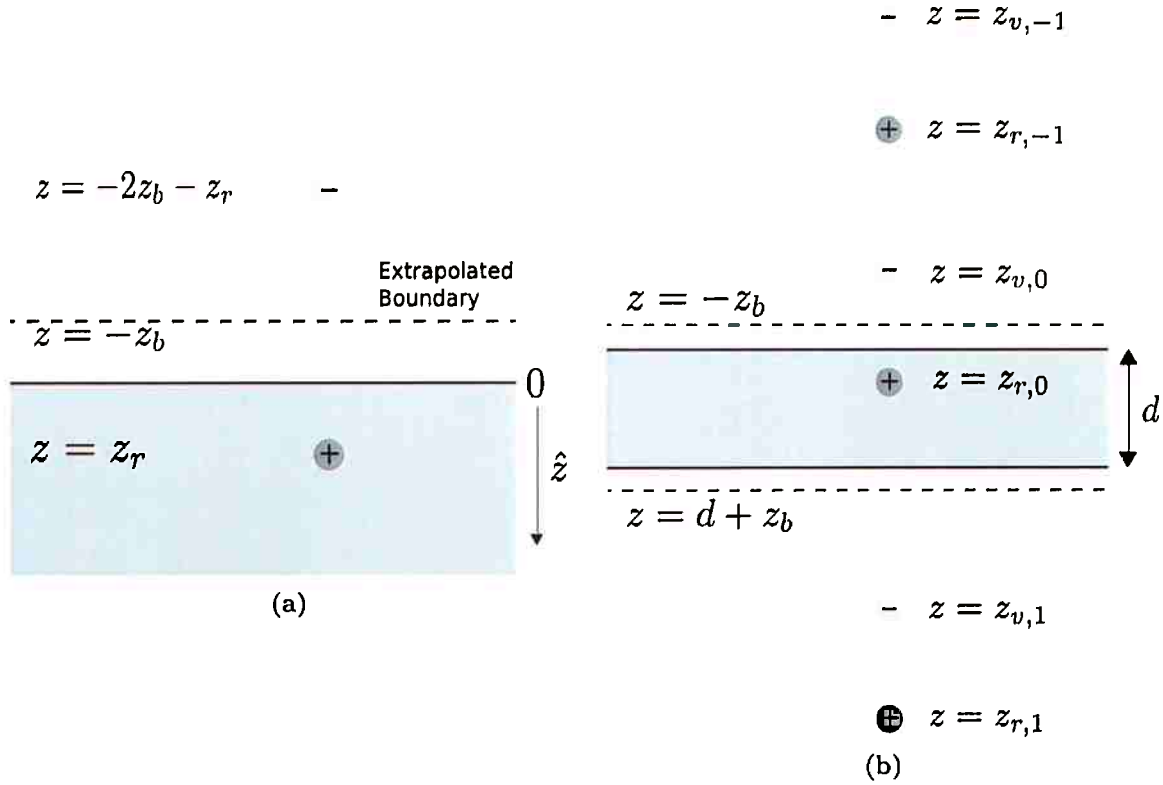
A new boundary condition is constructed for the bottom surface to overpass this problem, as shown in Figure 4.2. As with the top surface, the outward diffuse radiance is equal to the inward radiance reflected at the bottom surface:

$$\int_{\Omega^-} L_d(r, \vec{\omega})(\vec{\omega} \cdot \vec{n})d\vec{\omega} = F_{dr} \int_{\Omega^+} L_d(r, \vec{\omega})(\vec{\omega} \cdot -\vec{n})d\vec{\omega} \quad \text{at } z = d$$

resulting into:

$$\phi(r) + 2AD(\vec{n} \cdot \nabla)\phi(r) = 0 \quad \text{at } z = d, \tag{4.1}$$

which means that flux vanishes at depth $d + z_b$, which is z_b below the bottom surface of the slab, as seen in Figure 4.2b. This boundary is called the *bottom extrapolation boundary*.

$$- \quad z = z_{v,-1}$$

$$\oplus \quad z = z_{r,-1}$$

$$z = -2z_b - z_r \qquad -$$

Extrapolated
Boundary

$$- \quad z = z_{v,0}$$

$$z = -z_b$$

$$z = -z_b$$

$$0$$

$$\oplus \quad z = z_{r,0}$$

$$z = z_r \qquad \oplus$$

$$d$$

$$\hat{z}$$

$$z = d + z_b$$

(a)

$$- \quad z = z_{v,1}$$

$$\oplus \quad z = z_{r,1}$$

(b)

Figure 4.2: *Point source configuration: (a) Dipole configuration for semi-infinite slab and (b) multipole configuration for thin slabs [Don06]*

4.2.2 Multipole BSSRDF

To satisfy Equation 4.1, the top dipole is mirrored about $z = d + z_b$, which makes the net fluence from both dipoles result in zero at the bottom extrapolation boundary (lower dotted line in Figure 4.2b). To maintain the correction of the condition at the top condition boundary, $z = -z_b$ (top dotted line in Figure 4.2b), the bottom dipole needs to be mirrored about the top line. This process needs to be repeated infinitely in order to have both boundary conditions satisfied [DFG97, Wan98].

When the indices of refraction of the mediums above and below the slab are the same, the extrapolation distances will be the same, and the z-coordinates of the dipole sources will be given by:

$$z_{r,i} = 2i(d + 2z_b) + z_{r,0}$$
$$z_{v,i} = 2i(d + 2z_b) - z_{r,0} - 2z_b$$
$$\text{for } i = -n, ..., n$$

where d is the slab thickness, $z_{r,0}$ is the position of the original source at one MFP of depth [1], and $z_b = 2AD$ is the extrapolation distance. The even i variables try to satisfy the top condition, while odd i ones do the same for the bottom one. Finally, the diffuse reflectance profile due to $2n + 1$ dipoles is equal to the sum of their individual contributions.

$$R_d(r) = \sum_{i=-n}^{n} \frac{\alpha' z_{r,i}(1 + \sigma_{tr}d_{r,i})e^{-\sigma_{tr}d_{r,i}}}{4\pi d_{r,i}^3} - \frac{\alpha' z_{v,i}(1 + \sigma_{tr}d_{v,i})e^{-\sigma_{tr}d_{v,i}}}{4\pi d_{v,i}^3} \qquad (4.2)$$

where $d_{r,i} = \sqrt{r^2 + z_{r,i}^2}$ and $d_{v,i} = \sqrt{r^2 + z_{v,i}^2}$ are the distances to the dipole sources. Due to the

---

[1]$1MFP = 1/\sigma_t'$

fact that the contribution of each dipole decreases as the distance increases, the actual number of dipoles required depends on the slab thickness and the optical properties of the material.

4.2.3   Optimizations and limitations

The primary optimization brought by the multipole model is the capacity to support thin slabs. Figure 4.3 presents a piece of parchment illuminated from behind using Monte Carlo photon tracing, the dipole model and finally the multipole model. When evaluating the results of the dipole model one can perceive that it underestimates the amount of transmitted light while the multipole model matches the reference image, which was computed using Monte Carlo photon tracing.

(a)   (b)   (c)
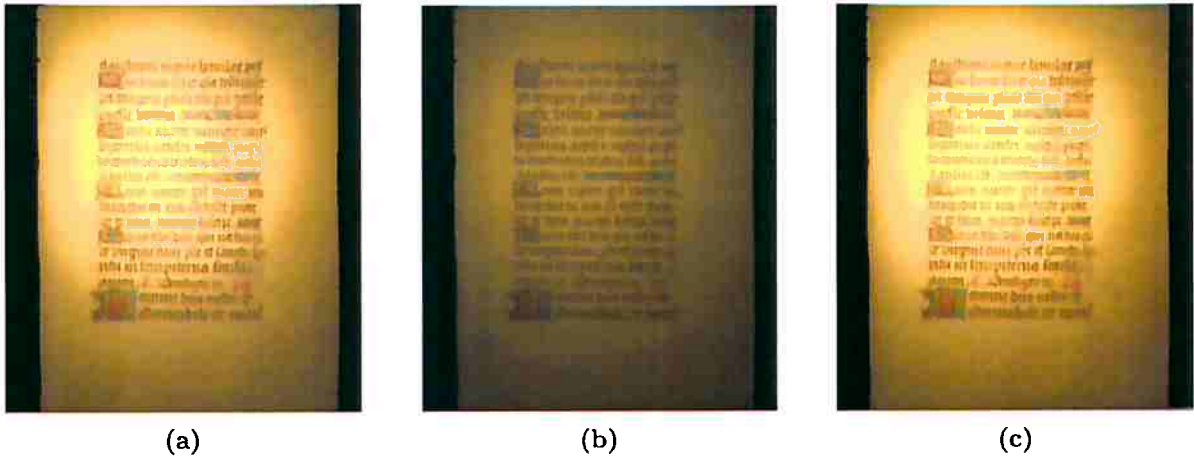
Figure 4.3: *Piece of parchment illuminated from behind using (a) Monte Carlo photon tracing as a reference, (b) the standard dipole model and (c) the multipole model [DJ05]*

The multipole model is also able to generate profiles for layered materials. Figure 4.4 presents the renderization of a human face using the dipole model with Jensen's parameters [JMLH01], using the multipole model with Tuchin's parameters [ToPoIE07], and, finally, an ear illuminated from behind using the multipole model.

(a)   (b)   (c)

Figure 4.4: *Human face rendered using the: (a) dipole model, (b) multipole model and (c) an ear illuminated from behind rendered using the multipole model [DJ05]*

Even though far-source reflectance and transmittance computation improved, near-source computation still presents a high error. Mainly because single scattering dominates radiant emittance in this area, and the dipole or multipole method fail to capture this.

4.3   The directional dipole diffusion model

The directional dipole model presents the first BSSRDF that takes into consideration the direction of incident illumination [FHK14]. Based on the solution of the diffusion equation for a ray of light in a highly scattering infinite medium [MSG05a, MSG05b].

Typically, radiance is split into three terms: reduced intensity, single scattering, and multiple scattering [HK93, JMLH01]. Instead, the directional dipole model uses the delta-Eddington (δE) approximation [JWW76]. Including the part of the single scattering that continues along the refracted ray in the reduced intensity term, $L_{\delta E}$, and the remaining single scattering in the diffusive part of the BSSRDF L_d [FHK14].

The modified reduced intensity term $L_{\delta E}$ maintains the definition of the original reduced intensity term, $L_{ri}(x) = L_i e^{-\tilde{\sigma}_t x}$, but uses a different set of scattering properties [JWW76]:

$$\tilde{\sigma}_t = \tilde{\sigma}_s + \sigma_a, \quad \tilde{\sigma}_s = \sigma_s(1 - g^2), \quad \tilde{g} = g/(g + 1)$$

4.3.1   Diffusion theory for a ray of light

The solution to the diffusion equation used in the directional dipole model works for a ray of light in an infinite medium. Solving the diffusion equation for this configuration gives:

$$\phi(r, \theta) = \frac{\Phi}{4\pi D} \frac{e^{-\sigma_{tr} r}}{r} \left(1 + 3D \frac{1 + \sigma_{tr} r}{r} \cos\theta\right) \tag{4.3}$$

where θ is the angle with the ray direction, as depicted in Figure 4.5 ($\cos\theta = ((x - x') \cdot \hat{z})/r$) [MSG05a, MSG05b].
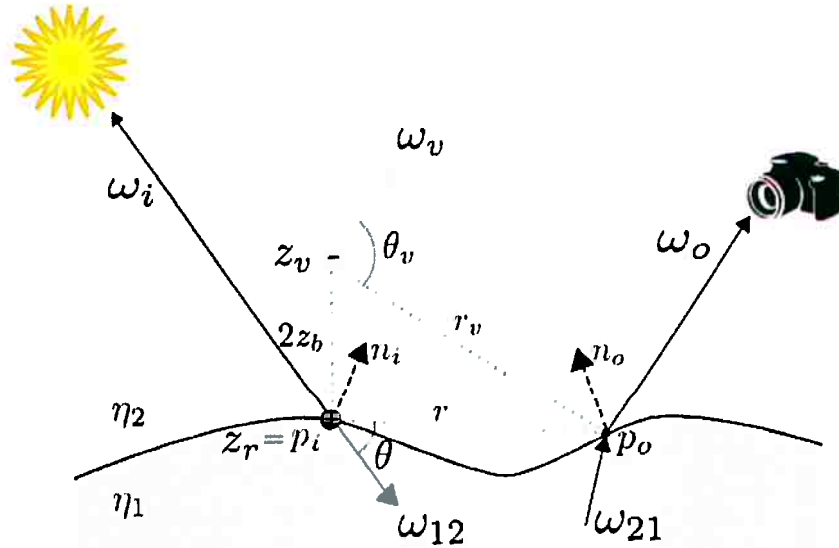
Figure 4.5: *Directional dipole configuration [HCJ13]*

4.3.2   Directional dipole BSSRDF

The radiant exitance is calculated using Kienle and Patterson's [KP97] approach, which combines the fluence and its derivative. The gradient of the fluence from the directional solution for a

monopole in an infinite medium is:

$$\nabla\phi_d^o = \frac{\Phi}{4\pi D}\frac{e^{-\sigma_{tr}r}}{r^3}\left(\vec{\omega_r}\,3D(1+\sigma_{tr}r)-(x-x_r)\,(1+\sigma_{tr}r)-\right.$$
$$\left.(x-x_r)\,3D\frac{3(1+\sigma_{tr}r)+(\sigma_{tr}r)^2}{r}\cos\theta\right),$$

where x_r is the location of the monopole and $\vec{\omega_r}$ is the direction of the incident ray after refraction. The diffuse radiant exitance for a monopole in an infinite medium is :

$$R_d^{monopole}((x-x_r),\vec{\omega_r},r) =$$
$$\frac{1}{4\pi}\frac{e^{\sigma_{tr}r}}{r^3}\left[C_\phi(\eta)\left(\frac{r^2}{D}+3(1+\sigma_{tr}r)(x-x_r)\cdot\vec{\omega_r}\right)-\right.$$
$$C_\mathbf{E}(\eta)\left(3D(1+\sigma_{tr}r)\vec{\omega_r}\cdot\vec{n}-\right.\qquad\qquad(4.4)$$
$$(1+\sigma_{tr}r)((x-x_r)\cdot\vec{n})+$$
$$\left.\left.(3D\frac{3(1+\sigma_{tr}r)+(\sigma_{tr}r)^2}{r^2}(x-x_r)\cdot\vec{\omega_r})(x-x_r)\cdot\vec{n}\right)\right],$$

where $\vec{n}$ is the surface's normal at the exitant point, and $C_\phi = \frac{1}{4}(1-2C_1(\eta))$ and $C_\mathbf{E} = \frac{1}{2}(1-3C_2(\eta))$. C_i are hemispherical integrals of the Fresnel reflectance F_r. The approximations of C_i are in appendix A.1.

For the dipole configuration, some changes were made. The extrapolated distance z_b, generally defined as $2AD$, changed to a new approximation, which is closer to the right z_b for weakly absorbing media with non-refractive boundary [Dav58]:

$$z_b = 2.131AD/\sqrt{\alpha'}$$

where α' is the reduced scattering albedo. When the real source is mirrored in the extrapolated boundary, the displacement of the virtual source becomes $2Az_b$.

Since the source is directional, it is also necessary to mirror the direction as well as the origin. Instead of using the *tangent plane*, defined by $\vec{n'}$, which is inaccurate when flat boundary assumption is violated, a modified tangent plane is used. The normal of this new plane is defined as:

$$\vec{n'^*} = \begin{cases} \vec{n} & ,\text{for } x = x' \\[2mm] \frac{x-x'}{|x-x'|}\times\frac{\vec{n'}\times(x-x')}{|\vec{n'}\times(x-x')|} & ,\text{otherwise} \end{cases}$$

The use of this plane eliminates the exaggerated directional effects caused by the assumption of a semi-infinite medium.

Other models use the average scattering displacement of the beam source as the representative location of the positive source ($z_r = 1/\sigma_t'$). Since the directional dipole aims to represent the actual light ray, no displacement is performed. This choice introduces a singularity in the model for $r = 0$ and creates an overestimation in the region close to the singularity. A correction is used to overpass this difficulty:

$$d_r^2 = \begin{cases} r^2 + D\mu_0(D\mu_0 - 2z_b\cos\beta) & ,\text{for } \mu_0 > 0 \text{ (front-lid)} \\[2mm] r^2 + 1/(3\sigma_t)^2 & ,\text{otherwise (back-lid)} \end{cases}$$

where $\mu_0 = -\vec{n} \cdot \vec{\omega_r}$, and the other cosine term is

$$\cos\beta = -\sin\theta \frac{r}{\sqrt{r^2 + z_b^2}} = -\sqrt{\frac{r^2 - ((x - x_r) \cdot \vec{\omega_r})^2}{r^2 + z_b^2}}$$

Using all these definitions, the final diffuse radiance profile of the directional dipole is:

$$R_d(x', \vec{\omega'}, x) = R_d^{monopole}(x - x_r, \vec{\omega_r}, d_r) - R_d^{monopole}(x - x_v, \vec{\omega_v}, d_v) \qquad (4.5)$$

where $x_r = x'$, $x_v = x' + 2Ad_c\vec{n}^{i*}$, $d_v = |x - x_v|$, and $\vec{\omega_v} = \vec{\omega_r} - 2(\vec{\omega_r} \cdot \vec{n}^{i*})\vec{n}^{i*}$ (see Figure 4.5).

Single scattering BSSRDF

The modified reduced intensity/single scattering term of the BSSRDF $S_{\delta E}$ can be indirectly defined by the radiance due to delta-Eddington's reduced intensity, and the transmitted radiance, L_t:

$$L_t(x', \vec{\omega_r}) = \eta^{-2} F_{12} L_i(x', \vec{\omega'}) \qquad (4.6)$$

where η is the relative refractive index and ω_r is the direction of the refracted ray given by the law of refraction applied to $\vec{\omega'}$. Then, the δE modified direct transmission emerging from the medium is:

$$L_{r,\delta E}(x, \vec{\omega}) = \eta^2 F_{21} e^{-\tilde{\sigma}_t s} L_t(x_{ri}, \omega_{-r}^-) \qquad (4.7)$$

where $x_{ri} = x - s\omega_{-r}^-$ is the only point on the surface that can contribute to this reduced intensity term, s is the distance from x to this point, and ω_{-r}^- is the direction of the ray from inside the medium refracting to the direction $\vec{\omega}$ according to the law of refraction. This term is easily evaluated using traditional ray-tracing [FHK14].

4.3.3 Optimizations and Limitations

The directional dipole model takes into consideration the direction of the incident ray that hits the surface of a translucent object, which provides a better simulation of light.

Figures 4.6 and 4.7 present a bunny made of white grapefruit juice and marble respectively. The bunnies are rendered using the standard dipole (left) and quantized-diffusion (second from left), with single scattering added using unbiased path tracing. There are also renderizations of the bunny using the directional dipole model (third from left) and using full path-tracing renderization (right), this last one is assumed to be the ground truth. The renderization of the bunny using the directional dipole model captures translucency effects that are present in the reference renderization. Though the inclusion of directional effects adds some costs in a rendering, the addition of single scattering balances these additional expenses, and outweighs them when light sources are small (or singular) [FHK14].

Figure 4.8 presents the squared differences (root-mean-square-error (RMSE) and structural similarity (SSIM)) of the renderizations of each model versus the path-tracing references.

The limitations of this model originate from the assumption of a planar semi-infinite medium. This assumption makes it difficult to represent objects that present thin features, or other complex geometries, accurately. This limitation is the reason to generate new models that extend the dirpole to lift these restrictions.
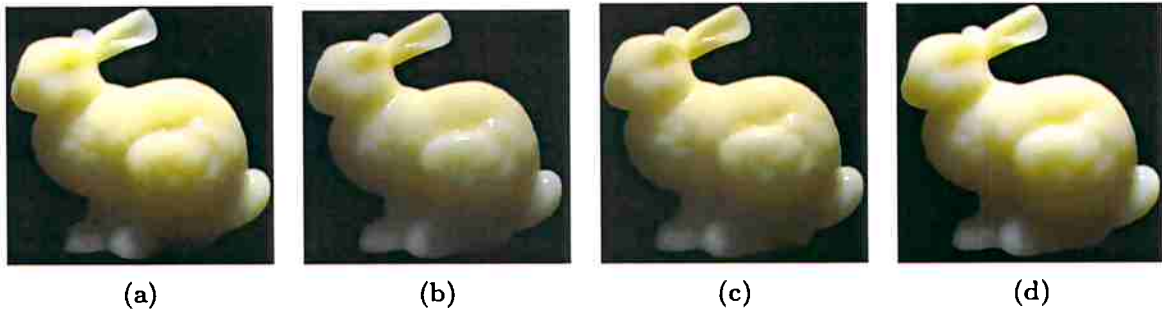
Figure 4.6: *Bunny made of white grapefruit juice rendered with (a) full path-tracing renderization (b) the standard dipole model, (c) the quantized-diffusion model and, finally, (c) the directional dipole model. Both the dipole and the quantized-diffusion model incorporating single-scattering calculated using path-tracing [FHK14]*
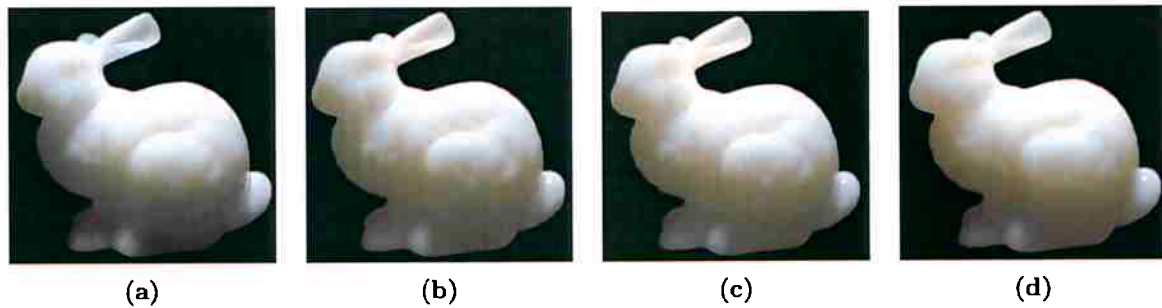
Figure 4.7: *Bunny made of marble rendered with (a) full path-tracing renderization (b) the standard dipole model, (c) the quantized-diffusion model and, finally, (c) the directional dipole model. Both the dipole and the quantized-diffusion model incorporating single-scattering calculated using path-tracing [FHK14]*
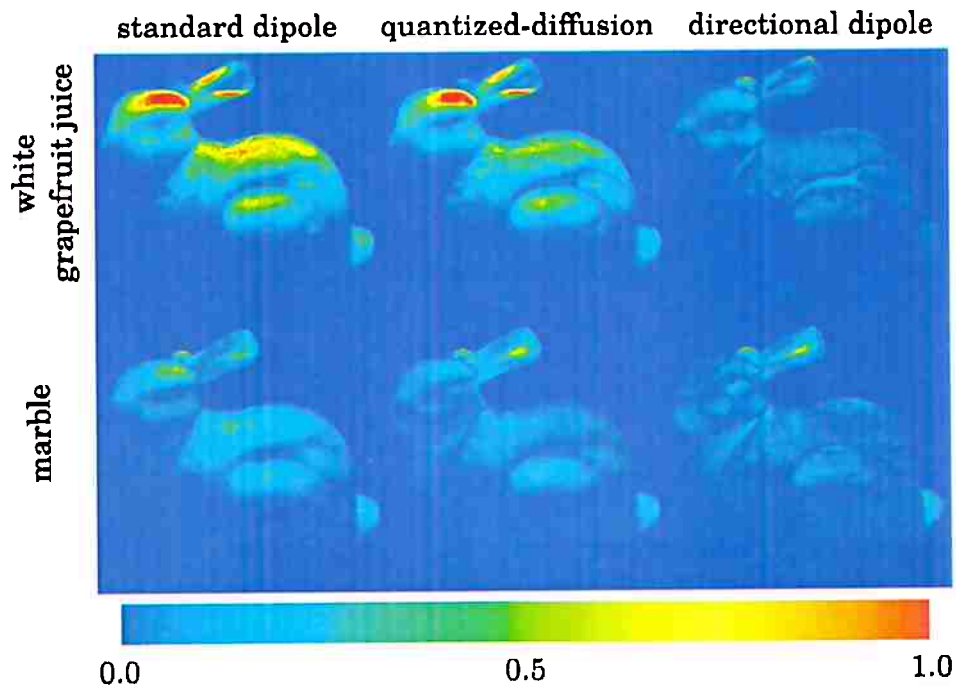
Figure 4.8: *Squared differences (root-mean-square-error (RMSE) and structural similarity (SSIM)) of the renderizations of each model versus the path-tracing references. [FHK14]*

Chapter 5

The directional multipole model

We have developed a new model that achieves a realistic simulation of light in translucent materials with geometrically thin volumes taking into account the direction of the incident ray. · This new model is an extension of the directional model, which takes into account the direction, position and normals of the incidence illumination ray as well as the normal of the exitant plane. This model achieves a great approximation using an analytic solution. We wanted to obtain this level of accuracy for thin volumes as well.

The principal limitation of the directional dipole model is the assumption that materials are semi-infinite. This means that the model assumes the rays of light that enter the surface will most likely be absorbed or they might return from the same face they entered. This assumption works well in thick geometries, with depth values around the centimeters or meters; however, the results when trying to model a thin slab, with depth values around the millimeters, are not as accurate. This restriction needs to be lifted to obtain a model that is able to represent complex volumes made of translucent materials.

Just like the multipole lifts this restriction from the dipole model, an extension of the directional dipole into a directional multipole would enable a better simulation of thin volumes.

5.1 Directional dipole kappa

Before creating a new model based on the directional dipole, we decided to compare it against the other models and improve its results. We realized the directional dipole model could be improved in the same way the dipole model was. With the help of an heuristic factor named *kappa*.

$$R_d(x', \vec{\omega}', x) = R_d^{monopole}(x - x_r, \vec{\omega}_r, d_r) - R_d^{monopole}(x - x_v, \vec{\omega}_v, d_v)$$

where $R_d^{monopole}$ was defined as:

$$R_d^{monopole}((x - x_r), \vec{\omega}_r, r) =$$
$$\frac{1}{4\pi} \frac{e^{\sigma_{tr}r}}{r^3} \left[C_\phi(\eta) \left(\frac{r^2}{D} + 3(1 + \sigma_{tr}r)(x - x_r) \cdot \vec{\omega}_r \right) - \right.$$
$$C_E(\eta) \left(3D(1 + \sigma_{tr}r)\vec{\omega}_r \cdot \vec{n} - \right.$$
$$(1 + \sigma_{tr}r)((x - x_r) \cdot \vec{n}) +$$
$$\left. \left. (3D\frac{3(1 + \sigma_{tr}r) + (\sigma_{tr}r)^2}{r^2}(x - x_r) \cdot \vec{\omega}_r)(x - x_r) \cdot \vec{n} \right) \right].$$

Adding a factor to modulate the overestimation around the surface, where single scattering dominates, a better result was obtained.

$$\kappa(r) = 1 - \exp^{-\sigma_t * r}$$

The *kappa* modulation factor is equal to the probability that light is not scattered before exiting the surface. This is why it works so well.

The results of adding the *kappa* factor can be seen in Figure 5.1. The original directional model is represented by the purple line and is the farthest away from the Monte Carlo simulation (assumed as the ground truth) represented by the black line, both when not taking into account single scattering (first column) and when it is taken into account (second column). Meanwhile, when the *kappa* factor is used, represented by the yellow line, to modulate the directional model, the results are the best analytic approximation. The photon-beam model, represented by the green line, uses Monte Carlo techniques that require an expensive integration of the solution along the refracted ray[FHK14].

(a) *Multi scattering*

(b) *Multi+single scattering*

(c) *Multi scattering closeup*

(d) *Multi+single scattering closeup*
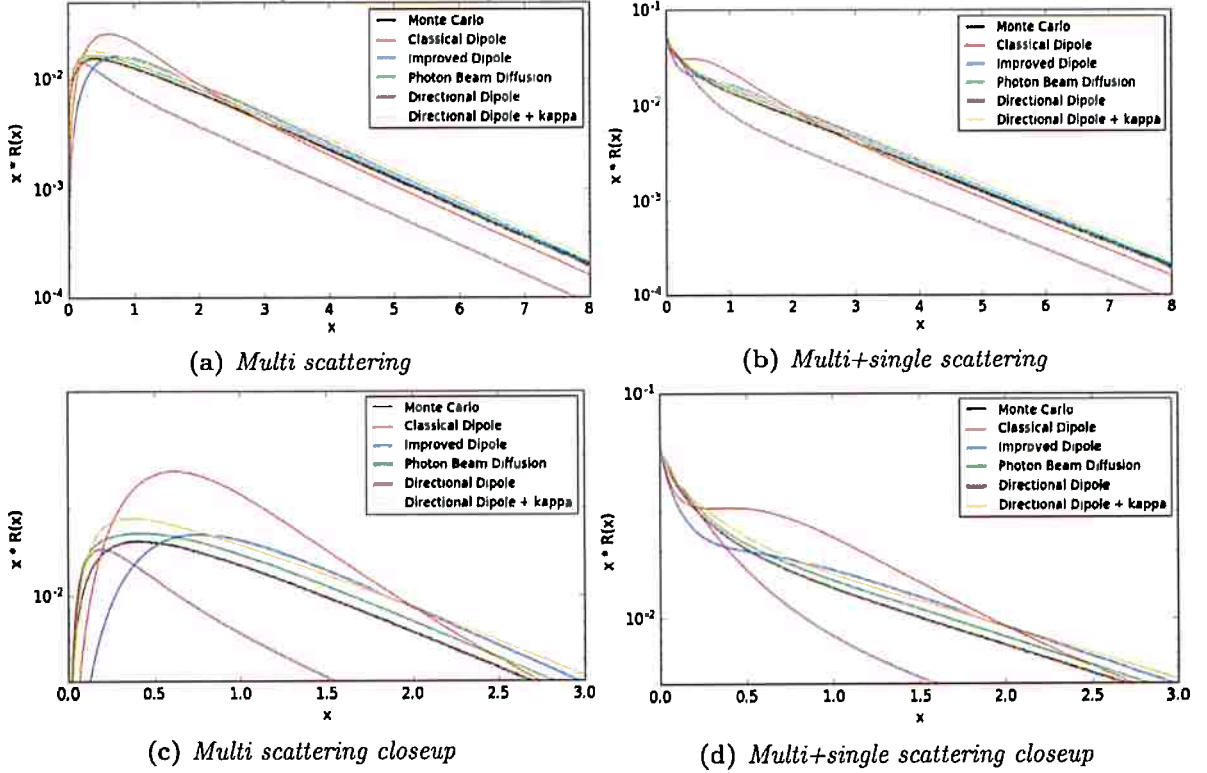
Figure 5.1: *Radiance profile for different diffusion based models with* $\sigma_s = 1$, $\sigma_a = 0.1$ *and* $g = 0$.

5.2   Directional multipole

To improve the directional dipole model, we added a new boundary condition to the bottom surface. Some of the light that enters the material gets transmitted, reducing the amount of light diffusing back to the surface, ignoring this situation overestimates the reflectance.

An important assumption is that diffuse light transmitted through the slab does no return, as was assumed in the multipole model. This means that the upward diffuse radiance is equal to the reflected downward one at the bottom surface:

$$\int_{\Omega-} L_d(r,\vec{\omega})(\vec{n}\cdot\vec{\omega})d\vec{\omega} = F_{dr}\int_{\Omega+} L_d(r,\vec{\omega})(-\vec{n}\cdot\vec{\omega})d\vec{\omega} \quad \text{at } z = d$$

Establishing that the flux vanishes at depth $d + z_{b,bottom}$, which is equal to the top boundary distance, except the refraction parameter, A, is calculated using the refractive index of the media underneath the bottom surface of the slab,

$$A_{bottom} = \frac{1 - C_{\mathbf{E}}(\eta_{bottom})}{C_\phi(\eta_{bottom})},$$

where C_E and C_ϕ depend upon the hemispherical integrals of the Fresnel reflectance C_i previously mentioned.
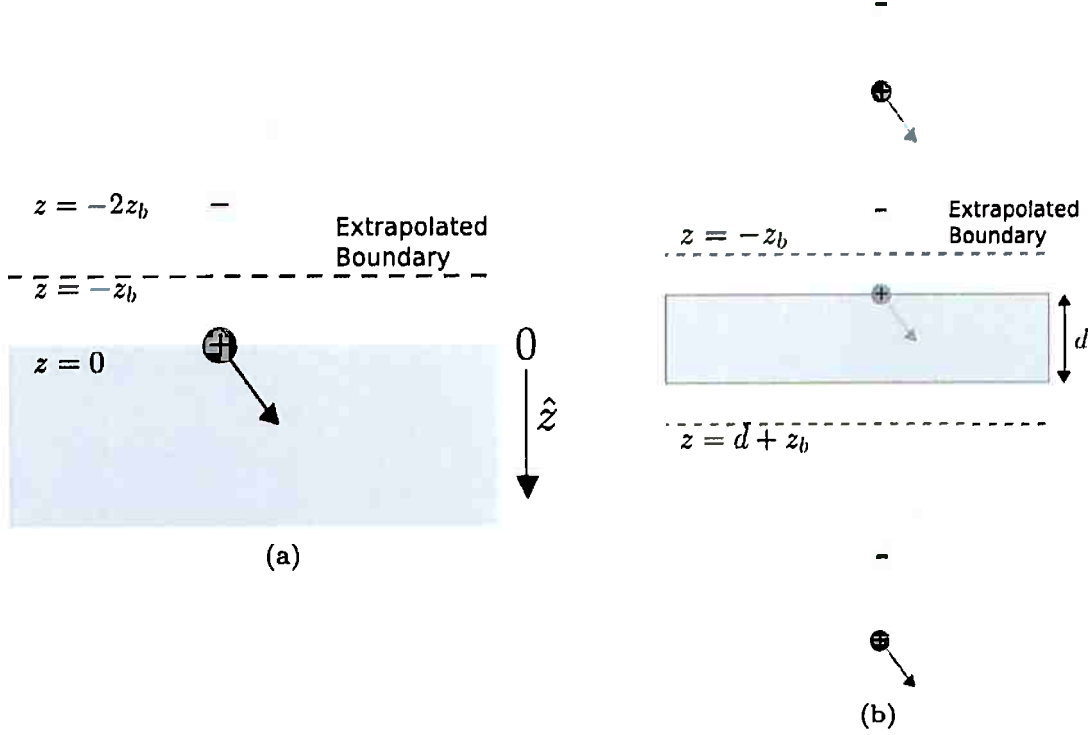
Figure 5.2: *Directional dipole configuration for semi-infinite slab (a) and directional multipole configuration for thin slabs(b) [Don06]*

Because of the method of images, the sources are mirrored about the top and bottom boundaries; both boundary conditions are simultaneously satisfied when there is an infinite array of dipoles [DFG97, Wan98], as depicted in Figure 5.2b. However, since the contribution of each source diminishes as the distance to the point of interest grows, an approximation of a finite number of sources achieves a good result. Assuming the surface is at the $z = 0$ plane, the $\vec{n}^{i*} = -\hat{z}$ and that $z_{r,0} = x'$, the positions of each dipole are, therefore:

$$p_{r,k} = \vec{z_{r,0}} - 2i(d + z_{b,top} + z_{b,bottom}) * \vec{n}^{i*}$$

$$p_{v,k} = \vec{z_{r,0}} - 2i(d + z_{b,top} + z_{b,bottom}) * \vec{n}^{i*} + 2z_{b,top} * \vec{n}^{i*}$$

$$\text{for } k = -\vec{n}, ..., \vec{n}$$

where each z_b is computed using the appropriate A. The reason why the $2i$ term is negated is because the $\vec{n}^{i*}$ is pointing in the opposite direction to the $\hat{z}$, as was previously stated. Negating these terms make the location of the sources correct according to the $\hat{z}$ axis.

When mirrored by the boundaries, the direction for each positive source light remains as ω_r and for each negative one as ω_v.

$$\omega_{r,i} = \omega_r$$

$$\omega_{v,i} = \omega_v$$

$$\text{for } i = -\vec{n}, ..., \vec{n}$$

5.2.1   Directional multipole BSSRDF

The reflectance due to $2n + 1$ dipoles used to satisfy both boundary conditions is equal to the summation of their individual contributions due to the linearity of illumination, giving us:

$$R_d(x', \vec{\omega'}, x) = \sum_{k=-n}^{n} R_d^{monopole}(x - p_{r,k}, \vec{\omega_r}, d_{r,k}) - R_d^{monopole}(x - p_{v,k}, \vec{\omega_v}, d_{v,k}) \qquad (5.1)$$

where $d_{r/v,k}$ are the distances to the dipole sources from a given point of interest x, and $p_{r/v,k}$ is the position of each source.

It is important to mention that when $n = 0$, the result of the directional multipole equation is the same as the directional dipole.

Chapter 6

Evaluation of the directional multipole model

We tested our new method by computing the radiance profiles values obtained for different optical parameters and a range of radial distances. These results were compared to those achieved by the improved dipole, the multipole, the photon-beam, and the directional dipole diffusion models.

The Monte Carlo implementation used as the ground truth was the *Monte Carlo for Multiple Layer media* of Lihong Wang et al[LL07]. The values of the absorption and scattering coefficients of the materials tested were the ones previously calculated by Jensen [JMLH01] and those calculated by Narasimhan et al. [NGD$^+$06]. They are listed in Table 6.1. We chose these materials because they exemplify the different configurations of scattering properties. The apple and marble have significantly bigger scattering values compared to their absorption counterparts. Meanwhile, ketchup has higher values in absorption than scattering. It is important to test our model in the different ranges of scattering properties; however, it is important to consider that multiple scattering is most significant in materials with an albedo close to one. In materials with lower albedos, the illumination is mostly characterized by single scattering.

	R	G	B
Apple	$\sigma_s = 2.29$ $\sigma_a = 0.003$ $\alpha = 0.99$ $mfp = 0.436$	$\sigma_s = 2.39$ $\sigma_a = 0.0034$ $\alpha = 0.99$ $mfp = 0.418$	$\sigma_s = 1.97$ $\sigma_a = 0.046$ $\alpha = 0.98$ $mfp = 0.496$
Ketchup	$\sigma_s = 0.18$ $\sigma_a = 0.061$ $\alpha = 0.75$ $mfp = 4.149$	$\sigma_s = 0.07$ $\sigma_a = 0.97$ $\alpha = 0.07$ $mfp = 0.962$	$\sigma_s = 0.03$ $\sigma_a = 1.45$ $\alpha = 0.02$ $mfp = 0.725$
Whole-milk	$\sigma_s = 2.55$ $\sigma_a = 0.0011$ $\alpha = 0.99$ $mfp = 0.392$	$\sigma_s = 3.21$ $\sigma_a = 0.0024$ $\alpha = 0.99$ $mfp = 0.311$	$\sigma_s = 3.77$ $\sigma_a = 0.014$ $\alpha = 0.99$ $mfp = 0.264$

Table 6.1: *Scattering properties of translucent materials: scattering and absorption coefficients in mm^{-1} (σ_s, σ_a), their albedo (α), and their mean free path mm (mfp)*

The results of these tests can be appreciated in Figures 6.1, 6.2 and 6.3, which shows the results for apple, ketchup and whole-milk materials. The closeup to head of the function in the apple and whole-milk materials can be appreciated in each of these figures.
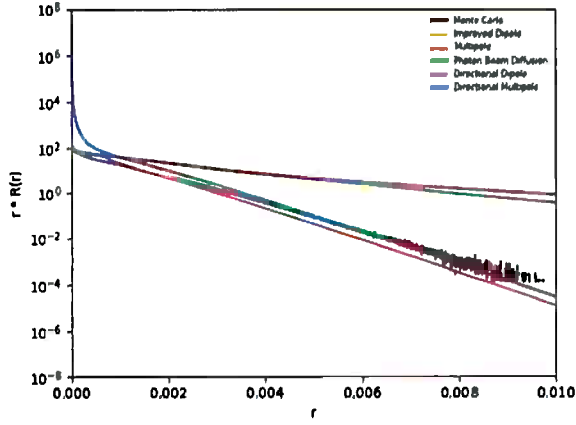
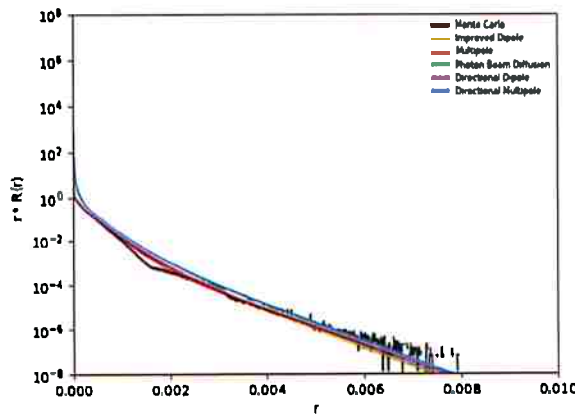(a) *Multi+single scattering, channel R*
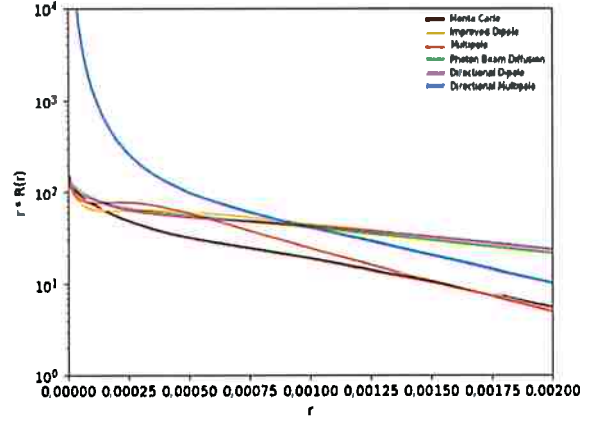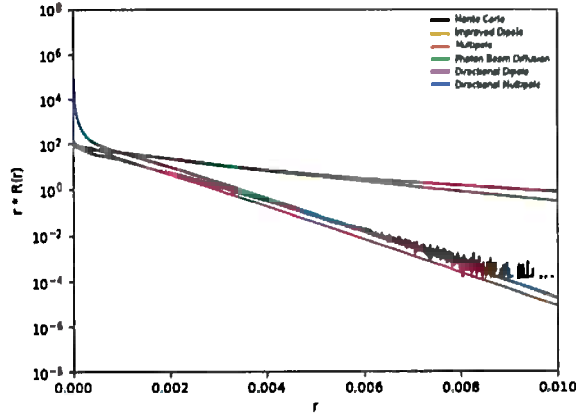
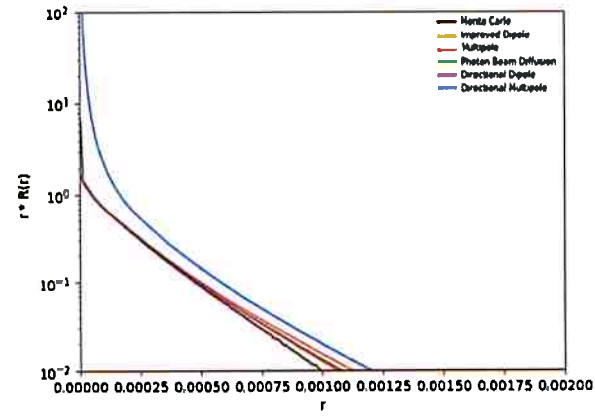(b) *Multi+single scattering closeup, channel R*

(c) *Multi+single scattering, channel G*
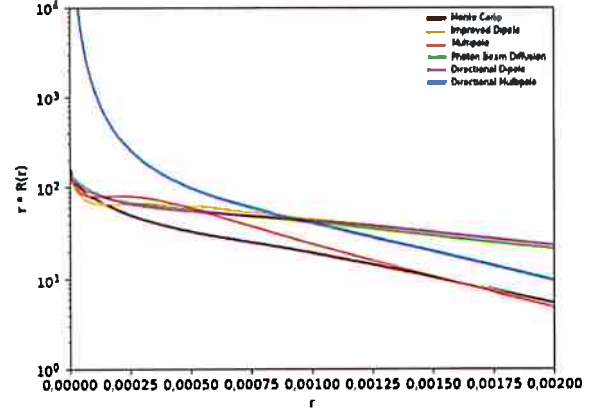
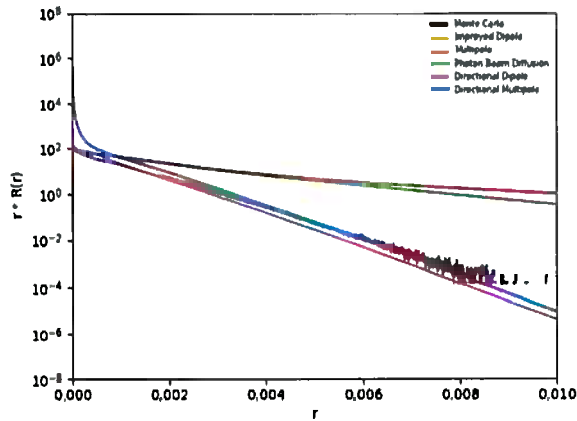(d) *Multi+single scattering closeup, channel G*
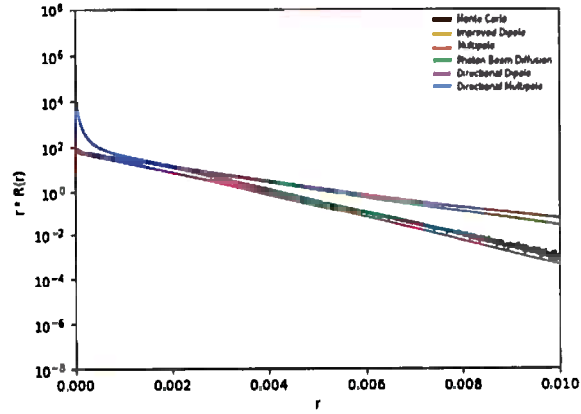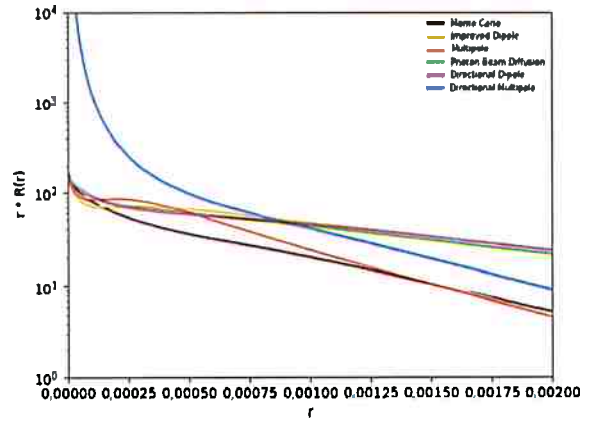

(e) *Multi+single scattering, channel B*
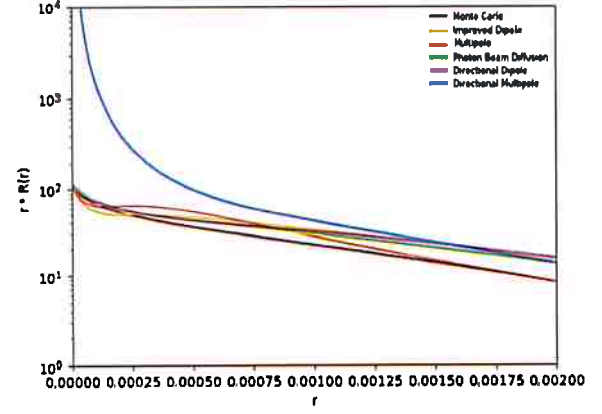
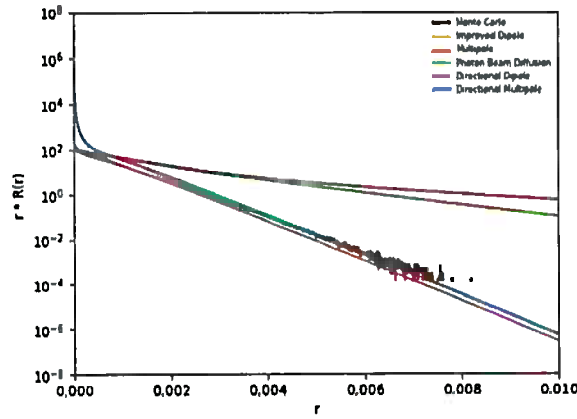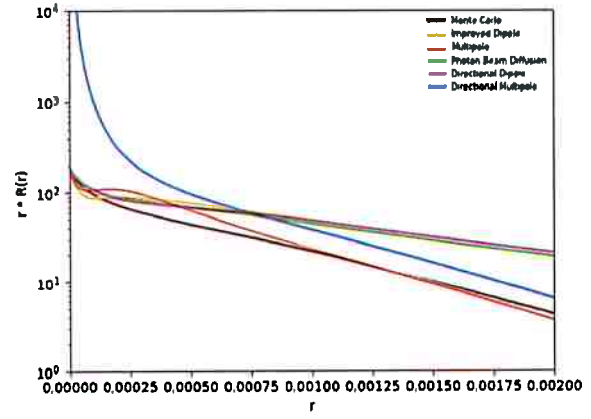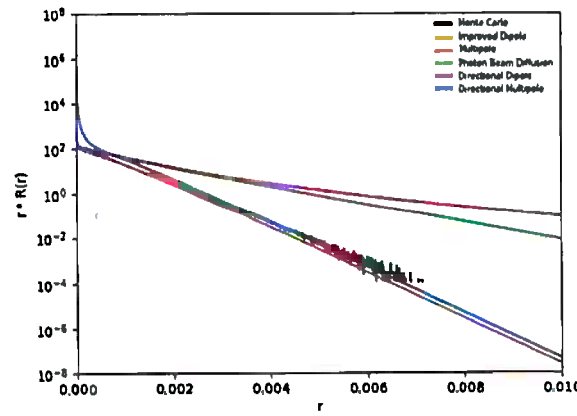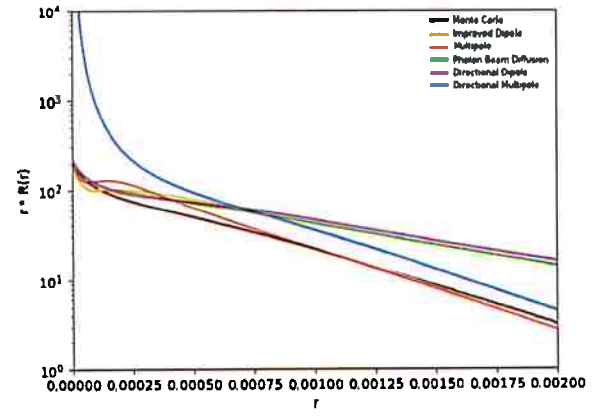(f) *Multi+single scattering closeup, channel B*

Figure 6.1: *Diffusion profile comparisons for an apple's RGB channels. (a) and (b) correspond to the R channel with $\sigma_s = 2.29$, $\sigma_a = 0.003$; (c) and (d) correspond to the R channel with $\sigma_s = 2.39$, $\sigma_a = 0.0034$; finally, (e) and (f) correspond to the R channel with $\sigma_s = 1.97$, $\sigma_a = 0.046$*
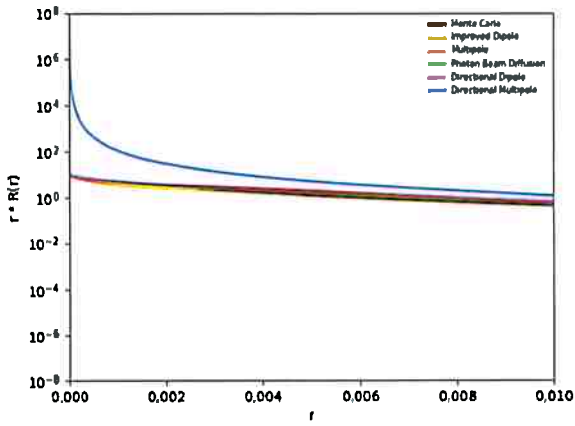
(a) *Multi+single scattering, channel R*
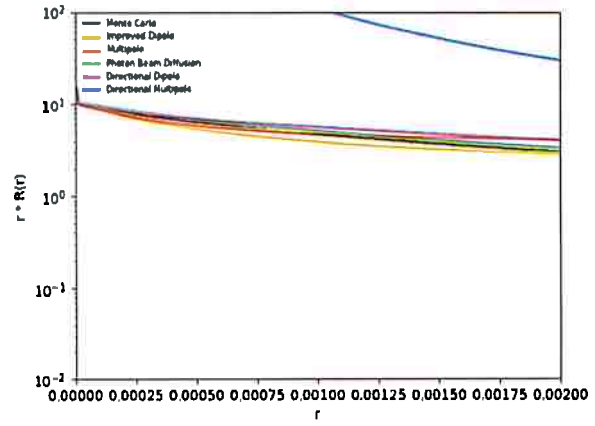
(b) *Multi+single scattering closeup, channel R*
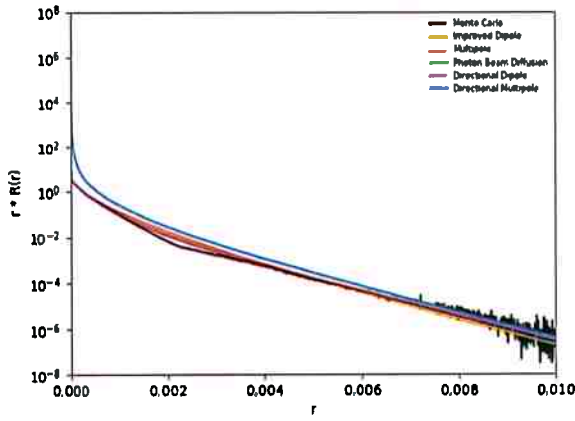
(c) *Multi+single scattering, channel G*
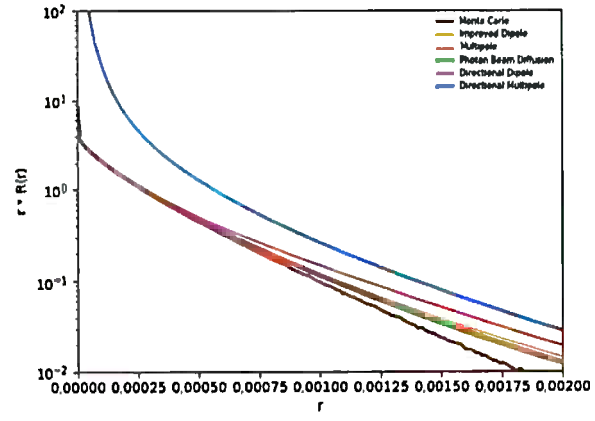
(d) *Multi+single scattering closeup, channel G*

(e) *Multi+single scattering, channel B*

(f) *Multi+single scattering closeup, channel B*

Figure 6.2: *Diffusion profile comparisons for an ketchup's RGB channels. (a) and (b) correspond to the R channel with $\sigma_s = 0.18$, $\sigma_a = 0.061$; (c) and (d) correspond to the R channel with $\sigma_s = 0.07$, $\sigma_a = 0.97$; finally, (e) and (f) correspond to the R channel with $\sigma_s = 0.03$, $\sigma_a = 1.45$*
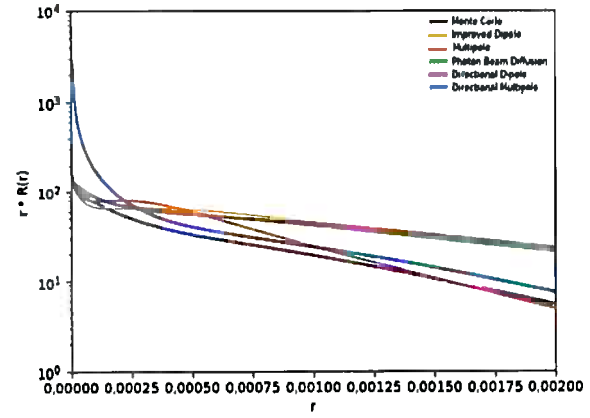
(a) *Multi+single scattering, channel R*
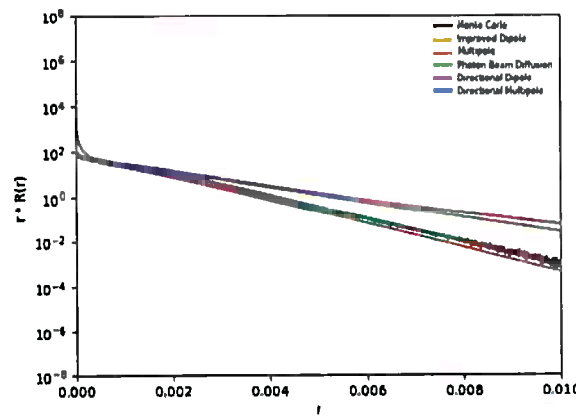

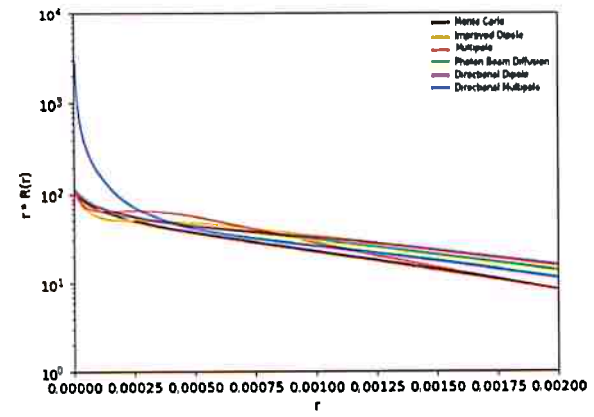(b) *Multi+single scattering closeup, channel R*

(c) *Multi+single scattering, channel G*

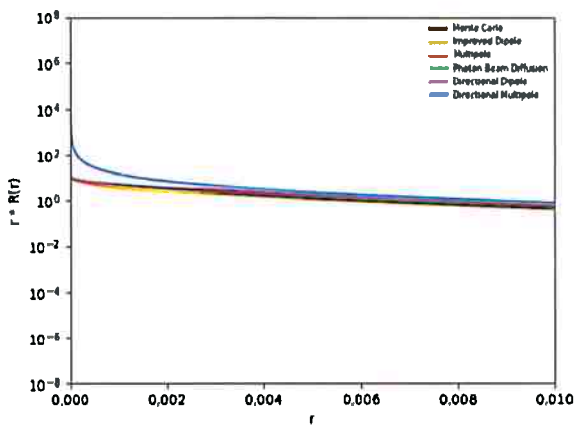(d) *Multi+single scattering closeup, channel G*
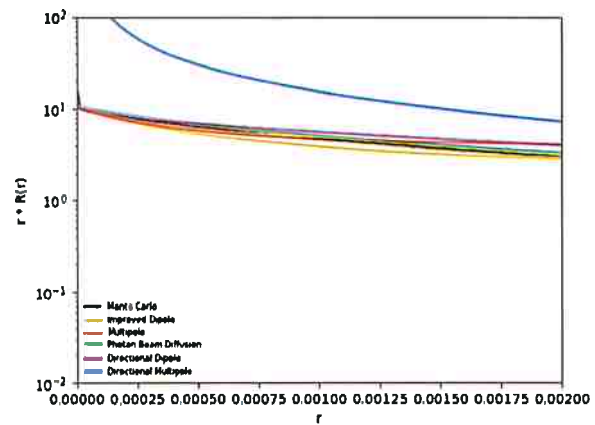

(e) *Multi+single scattering, channel B*
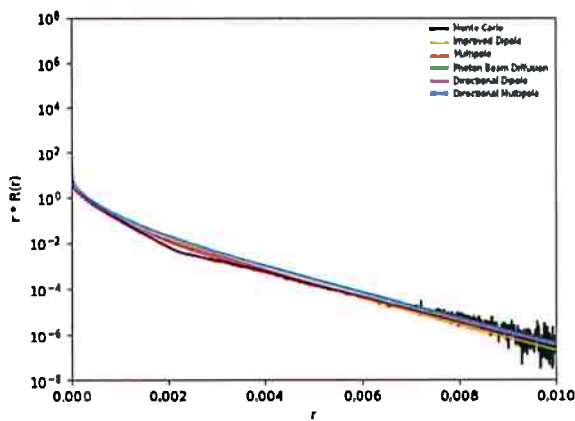

(f) *Multi+single scattering closeup, channel B*

Figure 6.3: *Diffusion profile comparisons for whole-milk's RGB channels. (a) and (b) correspond to the R channel with $\sigma_s = 2.55$, $\sigma_a = 0.0011$; (c) and (d) correspond to the R channel with $\sigma_s = 3.21$, $\sigma_a = 0.0024$; finally, (e) and (f) correspond to the R channel with $\sigma_s = 3.77$, $\sigma_a = 0.014$*

In these graphs the dipole based models: Dipole, Photon-Beam and the dirpole, represented by the yellow, green and purple, fail to represent the diffusion reflectance profile. They overestimate it because they assume the rays that penetrate the surface are absorbed or exit from the same face they entered. This, however, is not the case with the multipole based models: Multipole and directional multipole. As can be seen, the directional multipole model, represented by the blue line,

presents an overestimation when r is small. After this region its values improve to the point where it is the best fit.

In order to improve the result of our model we decided to apply a modified *kappa* factor to modulate the overestimation around the incident point. Our modified factor is defined as:

$$\kappa(r) = 1 - \exp^{-\sigma_t * r * 0.5}$$

When the modulating factor is used, the results improve significantly. The results of adding the *kappa* factor can be seen in Figures 6.4, 6.5 and 6.6.
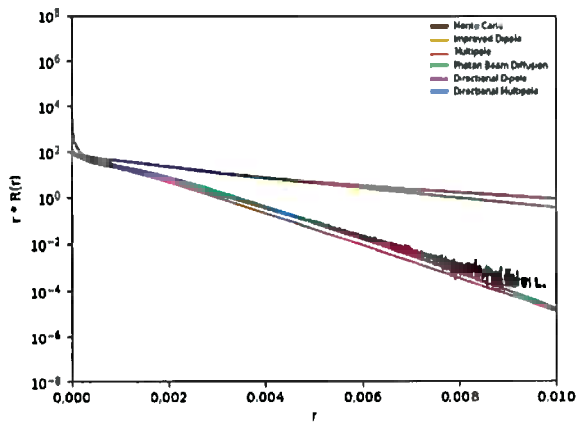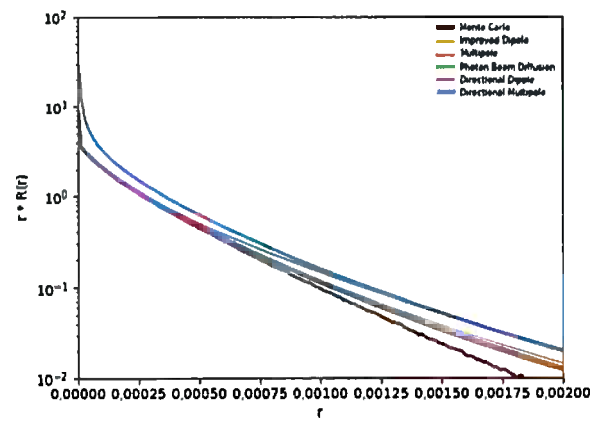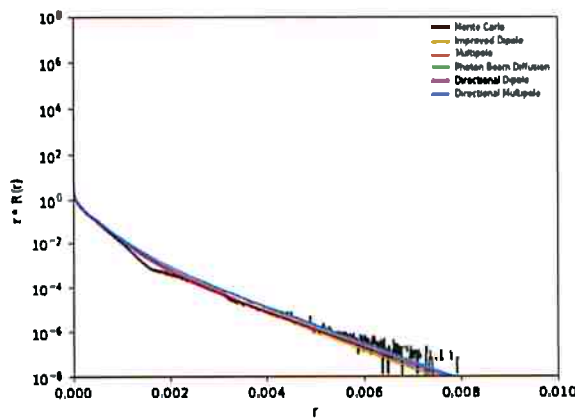
(a) *Multi+single scattering, channel R*
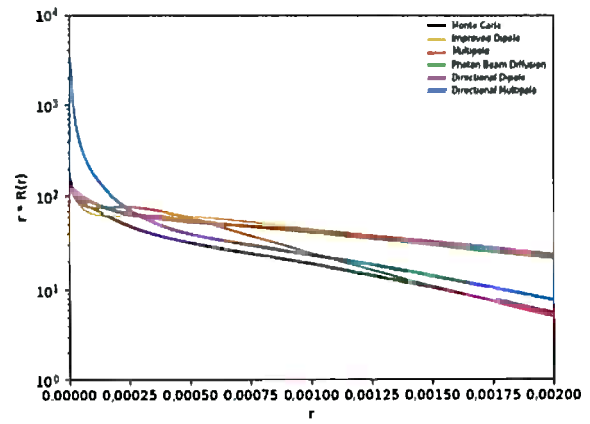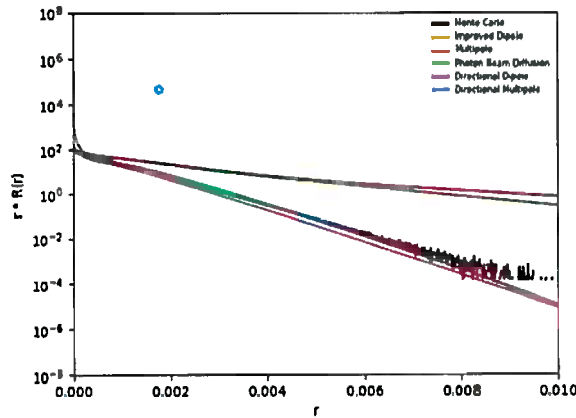
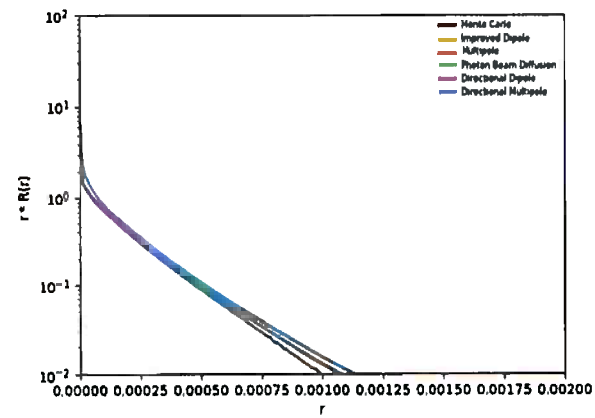(b) *Multi+single scattering closeup, channel R*

(c) *Multi+single scattering, channel G*

(d) *Multi+single scattering closeup, channel G*

(e) *Multi+single scattering, channel B*

(f) *Multi+single scattering closeup, channel B*

Figure 6.4: *Diffusion profile comparisons for an apple's RGB channels with factored model ($\kappa(r)$). (a) and (b) correspond to the R channel with $\sigma_s = 2.29$, $\sigma_a = 0.003$; (c) and (d) correspond to the R channel with $\sigma_s = 2.39$, $\sigma_a = 0.0034$; finally, (e) and (f) correspond to the R channel with $\sigma_s = 1.97$, $\sigma_a = 0.046$*

(a) *Multi+single scattering, channel R*

(b) *Multi+single scattering closeup, channel R*

(c) *Multi+single scattering, channel G*

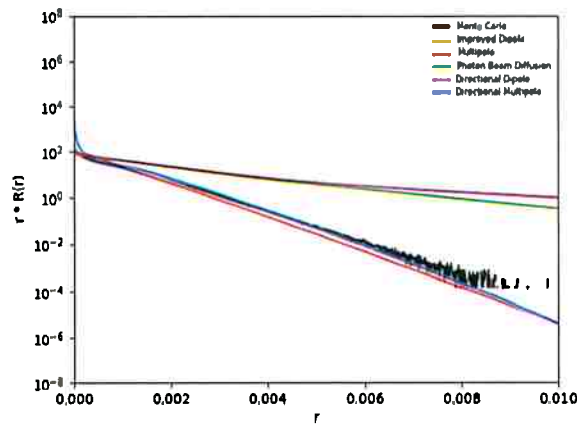(d) *Multi+single scattering closeup, channel G*
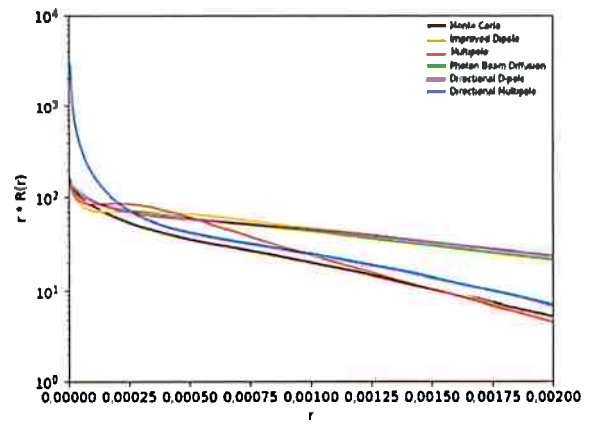

(e) *Multi+single scattering, channel B*
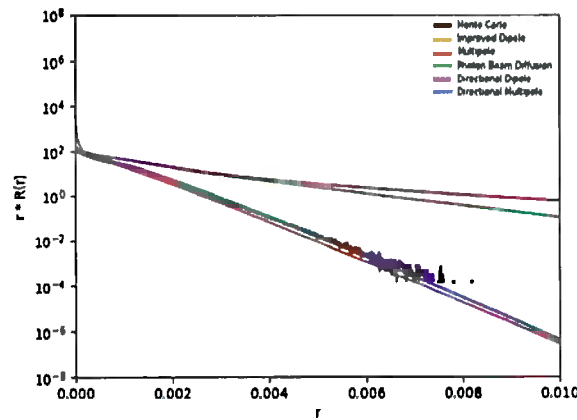

(f) *Multi+single scattering closeup, channel B*

Figure 6.5: *Diffusion profile comparisons for ketchup's RGB channels with factored model ($\kappa(r)$). (a) and (b) correspond to the R channel with $\sigma_s = 0.18$, $\sigma_a = 0.061$; (c) and (d) correspond to the R channel with $\sigma_s = 0.07$, $\sigma_a = 0.97$; finally, (e) and (f) correspond to the R channel with $\sigma_s = 0.03$, $\sigma_a = 1.45$*
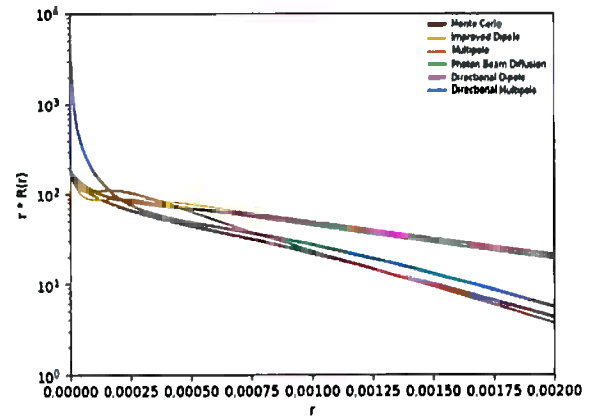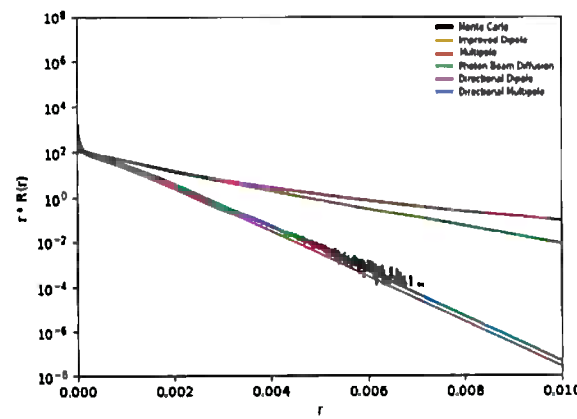
(a) *Multi+single scattering, channel R*

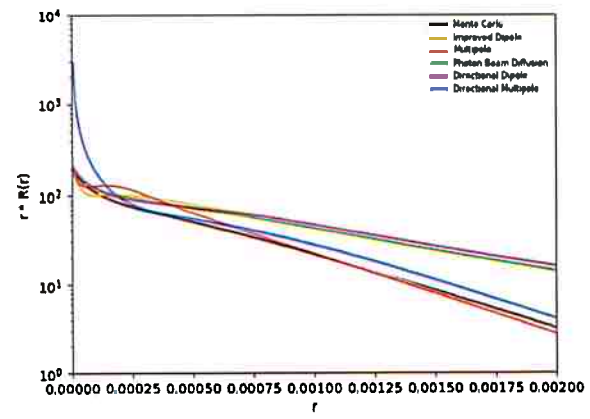(b) *Multi+single scattering closeup, channel R*

(c) *Multi+single scattering, channel G*

(d) *Multi+single scattering with closeup, channel G*

(e) *Multi+single scattering, channel B*

(f) *Multi+single scattering closeup, channel B*

Figure 6.6: *Diffusion profile comparisons for whole-milk's RGB channels with factored model ($\kappa(r)$). (a) and (b) correspond to the R channel with $\sigma_s = 2.55$, $\sigma_a = 0.0011$; (c) and (d) correspond to the R channel with $\sigma_s = 3.21$, $\sigma_a = 0.0024$; finally, (e) and (f) correspond to the R channel with $\sigma_s = 3.77$, $\sigma_a = 0.014$*

The *kappa* factor is a scale of the pdf that light is not scattered before exiting the surface. Adding this factor increases the accuracy of our model, making it the closest one to the Monte Carlo simulation, represented by the black line.

Until now we used the distance between the real source to the output point as part of our calculation. However, the directional dipole model uses a correction to control a singularity present

when $r = 0$.

$$d_r^2 = \begin{cases} r^2 + D\mu_0(D\mu_0 - 2z_b\cos\beta) & \text{, for } \mu_0 > 0 \text{ (front-lid)} \\ \\ r^2 + 1/(3\sigma_t)^2 & \text{, otherwise (back-lid)} \end{cases}$$

We use this approximation when the distance between the input and output point is less than $2/\sigma_t$. This generates a small step in the values obtained around $2/\sigma_t$, but the magnitude of this step does not affect the final result, it also could be smoothed by the means of another factor, but it was not valued as important. The range of application of this correction was found through a series of tests with different materials. The results of using this correction can be seen in Figures 6.7, 6.8 and 6.9.
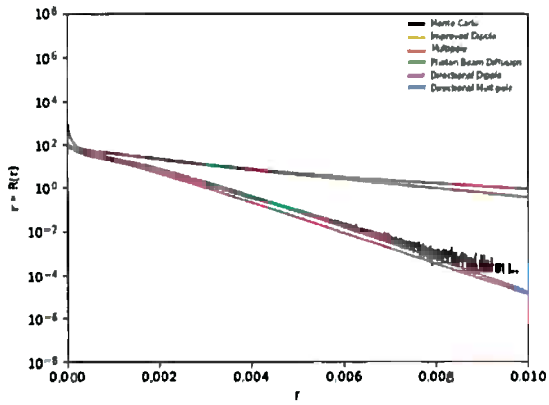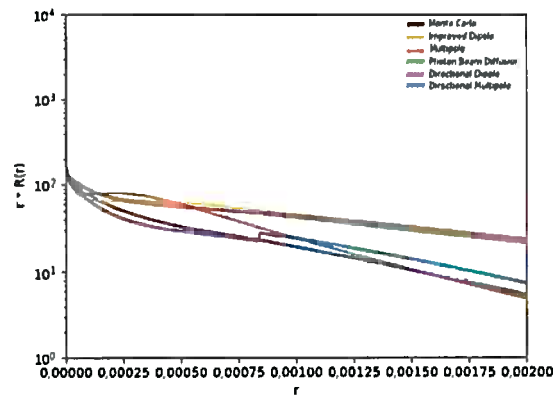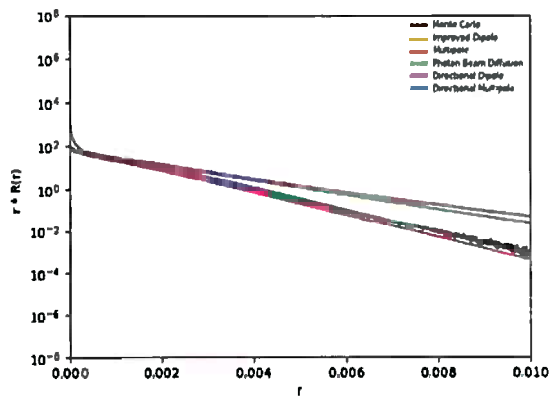
(a) *Multi+single scattering, channel R*
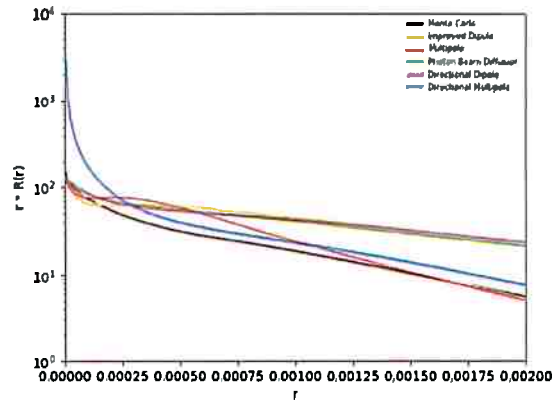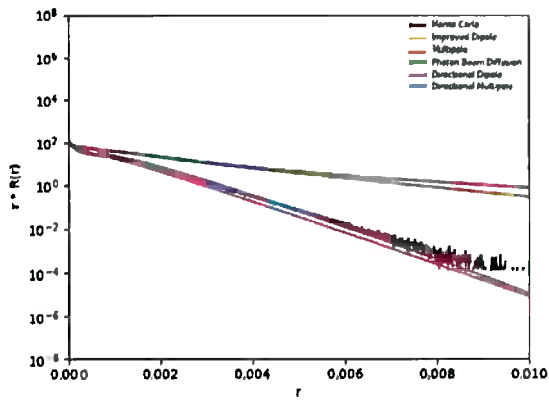
(b) *Multi+single scattering closeup, channel R*

(c) *Multi+single scattering, channel G*

(d) *Multi+single scattering closeup, channel G*

(e) *Multi+single scattering, channel B*
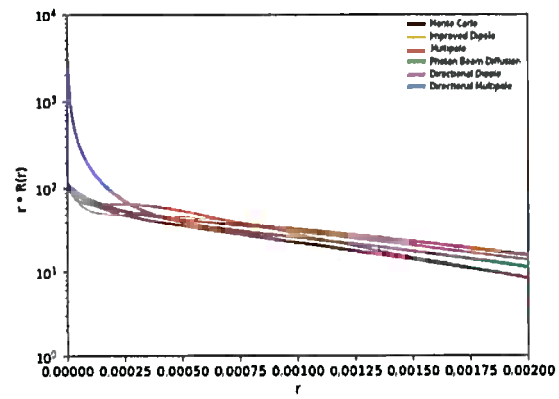
(f) *Multi+single scattering closeup, channel B*

Figure 6.7: *Diffusion profile comparisons for an apple's RGB channels with factored model ($\kappa(r)$) and corrected $d(r)$. (a) and (b) correspond to the R channel with $\sigma_s = 2.29$, $\sigma_a = 0.003$; (c) and (d) correspond to the R channel with $\sigma_s = 2.39$, $\sigma_a = 0.0034$; finally, (e) and (f) correspond to the R channel with $\sigma_s = 1.97$, $\sigma_a = 0.046$*
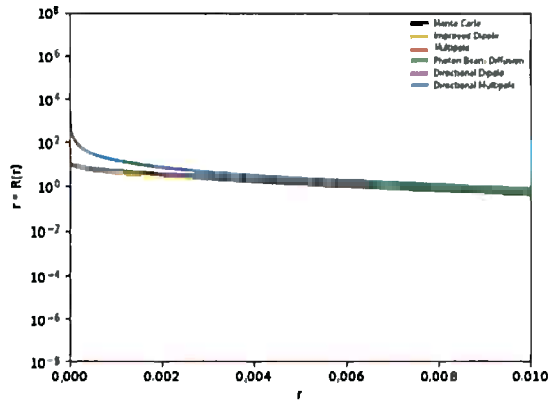
(a) *Multi+single scattering, channel R (σ_s = 0.18, σ_a = 0.061)*

(b) *Multi+single scattering closeup, channel R*

(c) *Multi+single scattering, channel G (σ_s = 0.07, σ_a = 0.97)*

(d) *Multi+single scattering closeup, channel G*

(e) *Multi+single scattering, channel B (σ_s = 0.03, σ_a = 1.45)*
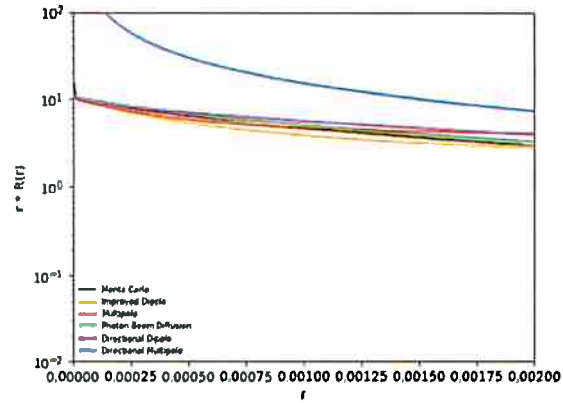
(f) *Multi+single scattering closeup, channel B*

Figure 6.8: *Diffusion profile comparisons for ketchup's RGB channels with factored model ($\kappa(r)$) and corrected $d(r)$. (a) and (b) correspond to the R channel with σ_s = 2.29, σ_a = 0.003; (c) and (d) correspond to the R channel with σ_s = 2.39, σ_a = 0.0034; finally, (e) and (f) correspond to the R channel with σ_s = 1.97, σ_a = 0.046*
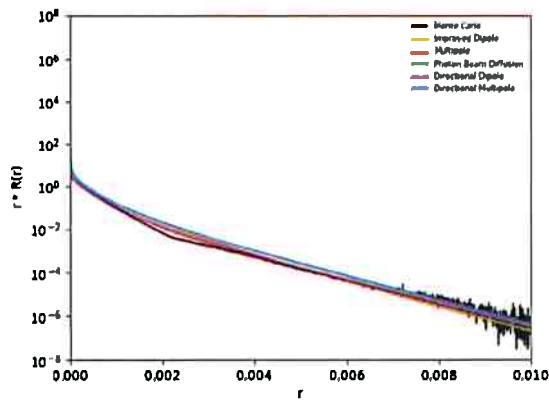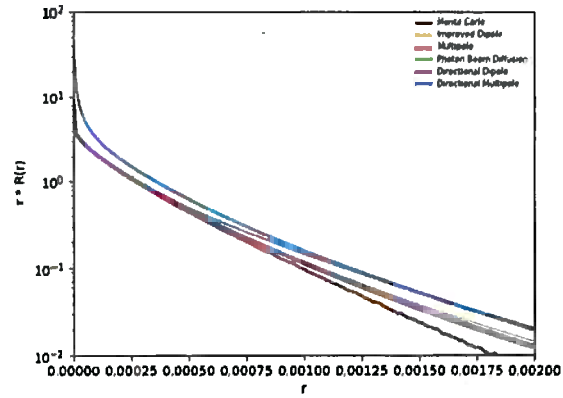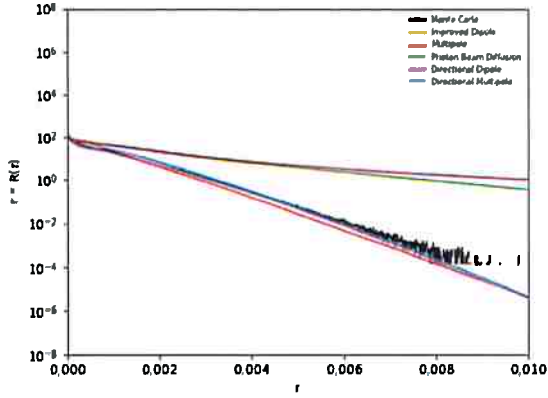
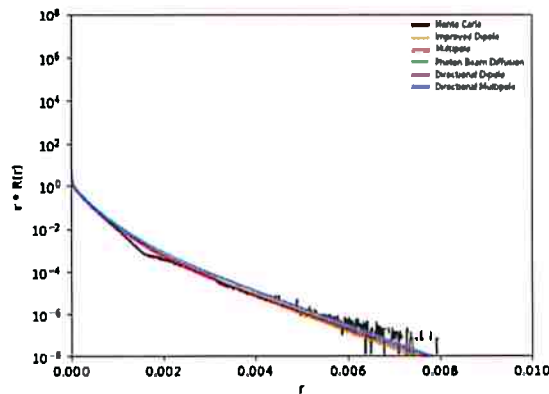(a) *Multi+single scattering, channel R (σ_s = 2.55, σ_a = 0.0011)*
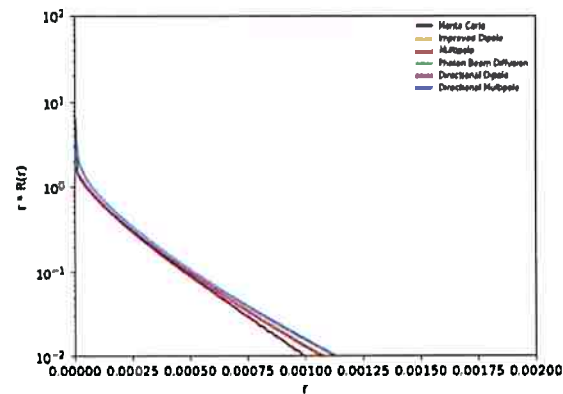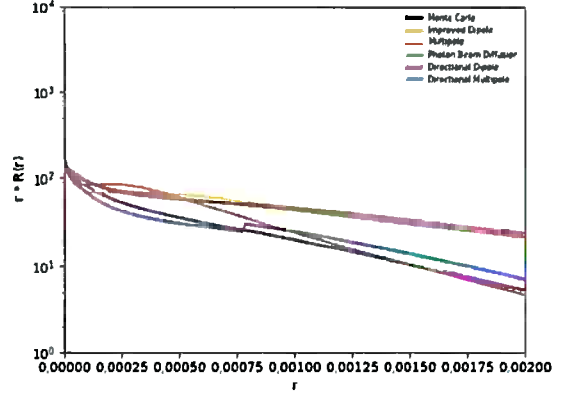
(b) *Multi+single scattering closeup, channel R*
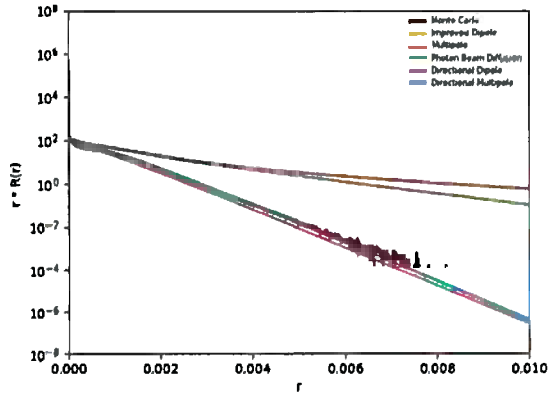
(c) *Multi+single scattering, channel G (σ_s = 3.21, σ_a = 0.0024)*
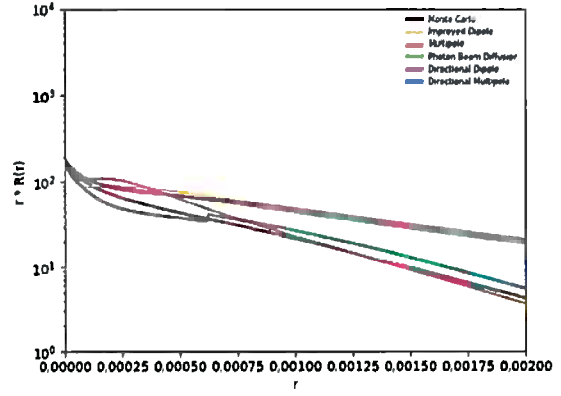
(d) *Multi+single scattering closeup, channel G*
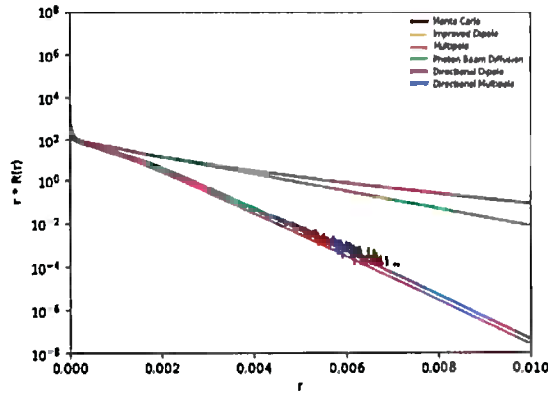
(e) *Multi+single scattering, channel B (σ_s = 3.77, σ_a = 0.014)*
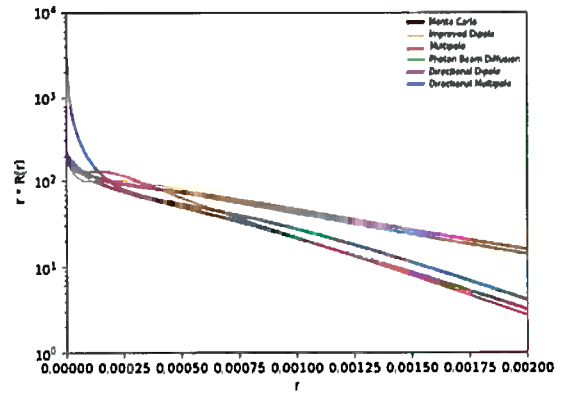
(f) *Multi+single scattering closeup, channel B*

Figure 6.9: *Diffusion profile comparisons for whole-milk's RGB channels with factored model ($\kappa(r)$) and corrected $d(r)$. (a) and (b) correspond to the R channel with σ_s = 2.55, σ_a = 0.0011; (c) and (d) correspond to the R channel with σ_s = 3.21, σ_a = 0.0024; finally, (e) and (f) correspond to the R channel with σ_s = 3.77, σ_a = 0.014*

6.1   Rendered image evaluation

The following images were rendered using the photo-beam model, the directional dipole model, the multipole model and our directional multipole. They are visual representations of the reflectance diffusion profile. We are using the results of the multipole model as the ground truth since this is the model that best represented thin slabs. For our tests, we used homogeneous materials such as grapefruit juice, ketchup and marble, using the optical parameters previously detailed in Table 6.1. The methods used for analysis are **Mean squared error** (MSE), **Structural similarity** (SSIM) and finally the **Visual Difference Predictor for HDR images standard** (HDR-VDP-2). The MSE gives a numerical punctuation of dissimilarity between two images, the smaller this value is, the more similar they are. This values is equal to the average of the squares of the deviations between these images. The SSIM indicator produces an image that shows darker color in the regions with values more distant to each other. Meanwhile, the HDR-VDP-2 allows us to compare a pair of images and measure the probability that the differences between the images is visible for an average observer; red denotes great probability and blue less.
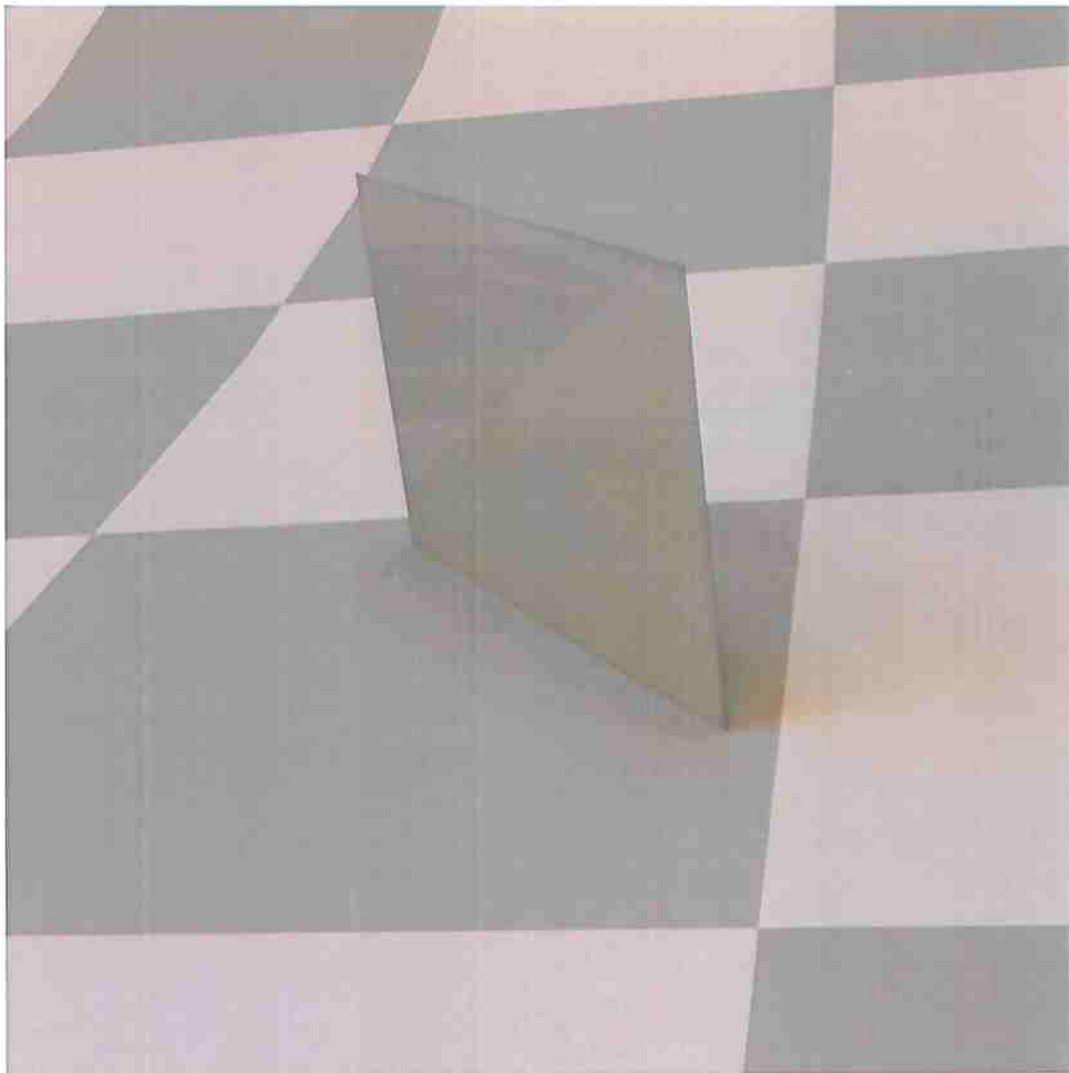
Figure 6.10: *Directional multidirpole grapefruit*
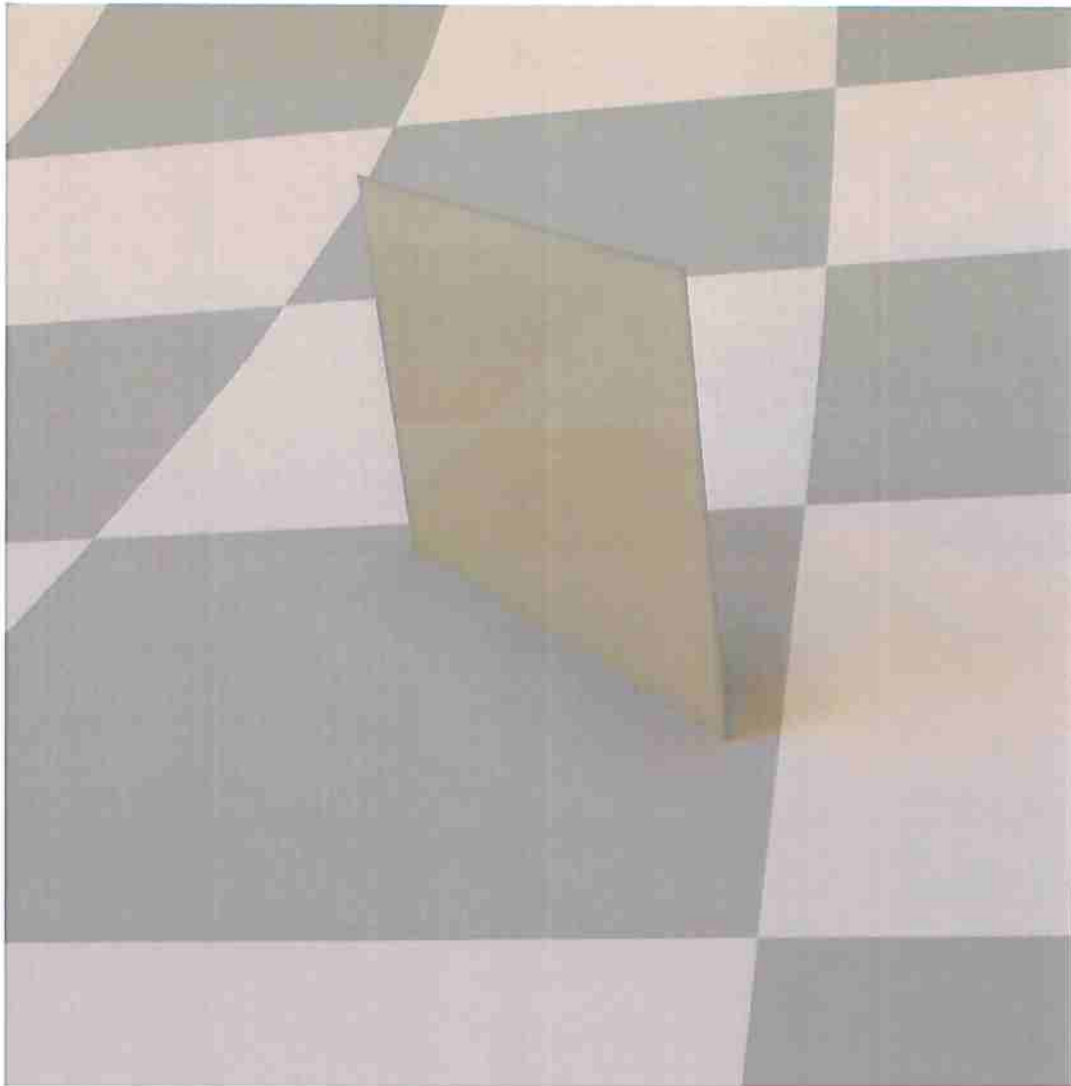
Figure 6.11: *Multipole grapefruit*

As we can see the results from the directional multipole model come closer to the results from the multipole model. The directional dipole and photon-beam and directional dipole are more closely related to each other since they share the same assumptions.

Mean Squared Error   Structural Similarity   HDR-VDP-2

(a) *MSE:75.47546*   (b) *SSIM:0.98979*   (c)

(d) *MSE:103.94792*   (e) *SSIM:0.98707*   (f)

(g) *MSE:63.37565*   (h) *SSIM:0.99001*   (i)
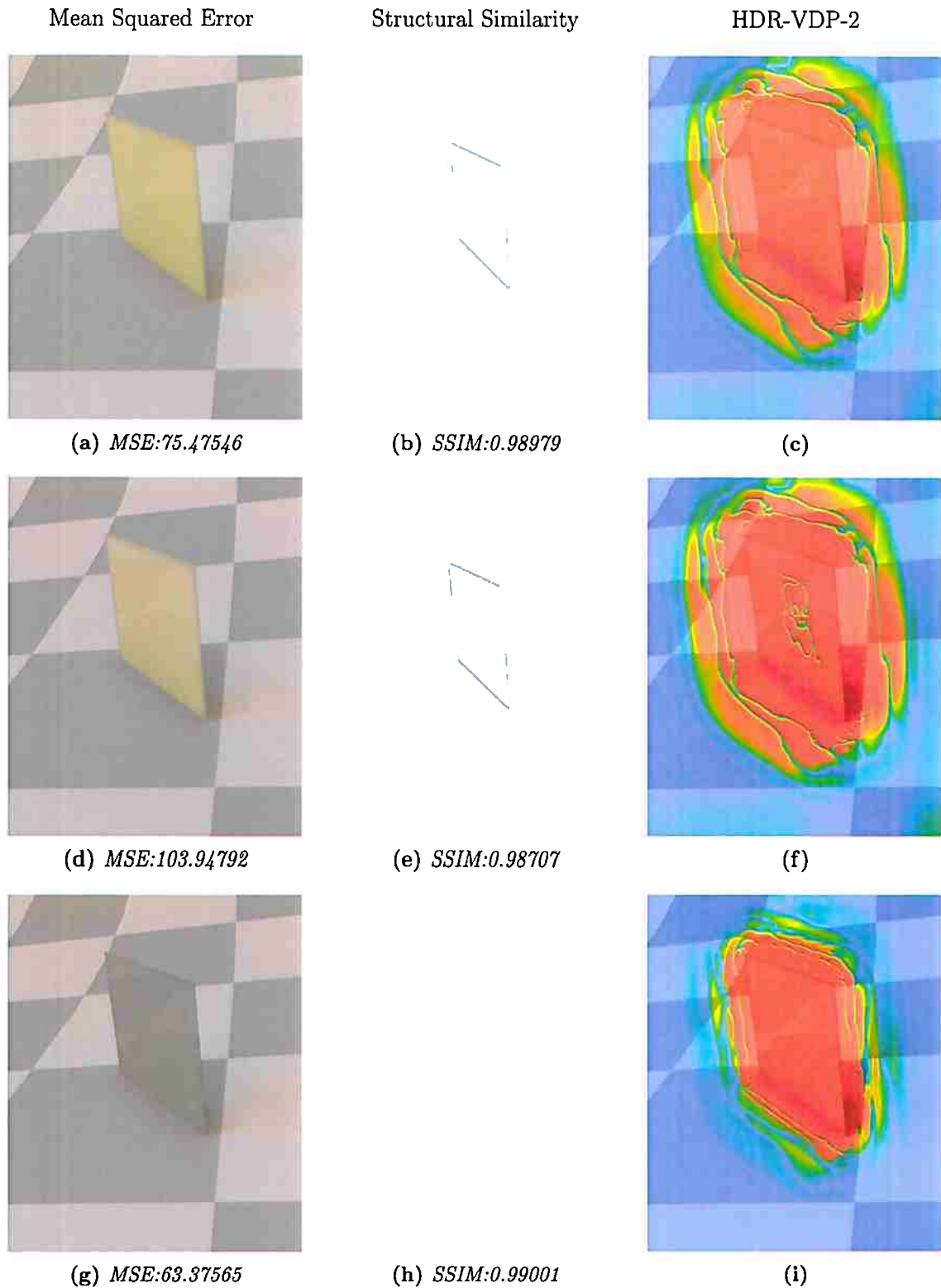
Table 6.2: *Comparing reflection profile results for grapefruit to the results obtained by the multipole model; first line corresponds to the diffusion beam, second line is the directional dipole, finally, the third one corresponds to the directional multipole. The first column shows the results for each model and their Mean Square Error, the second column the Structural Similarity results, and, finally, the third one the Visual Difference Predictor*
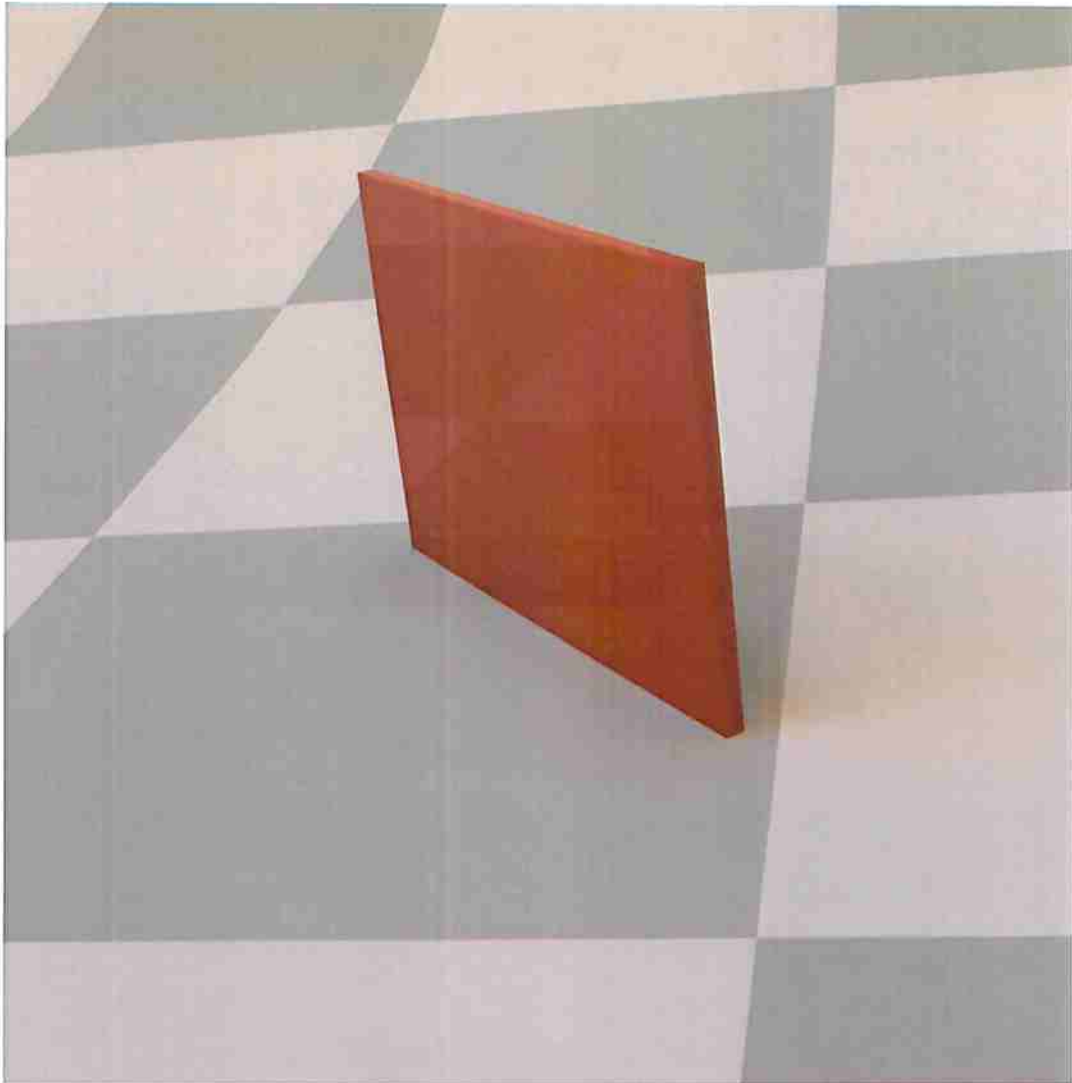
Figure 6.12: *Directional multidirpole ketchup*
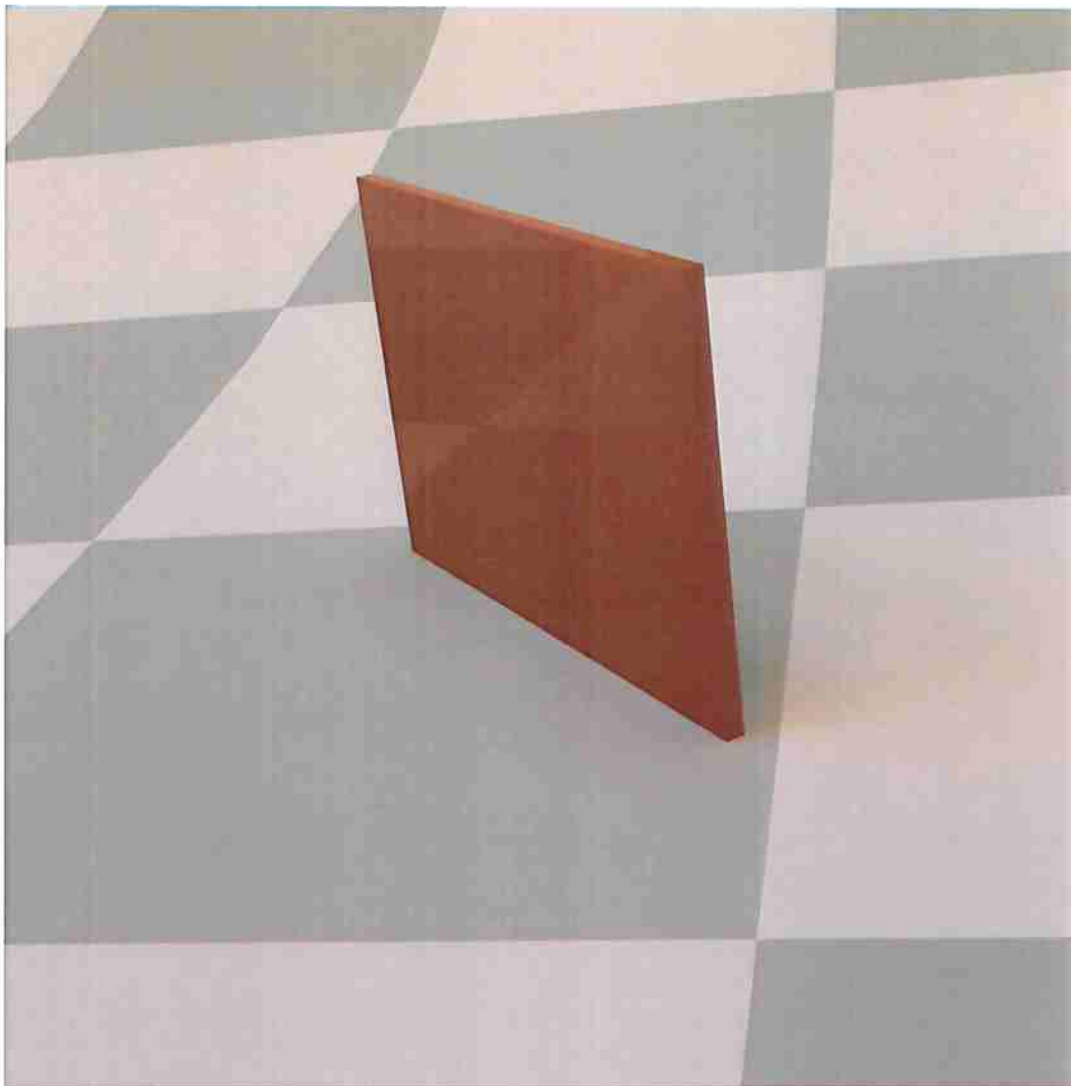
Figure 6.13: *Multipole ketchup*

As we can see the results from the ketchup material do not differ much from one another. This is because the resulting profile from the diffuse reflectance is mostly influenced by single scattering. Since single scattering is computed in the same way for all models, the resulting values are closely related.

Mean Squared Error	Structural Similarity	HDR-VDP-2

(a) *MSE:1.92571*   (b) *SSIM:0.99897*   (c)

(d) *MSE:10.65553*   (e) *SSIM:0.99779*   (f)

(g) *MSE:7.28456*   (h) *SSIM:0.98923*   (i)

Table 6.3: *Comparing reflection profile results for ketchup to the results obtained by the multipole model; first line corresponds to the diffusion beam, second line is the directional dipole, finally, the third one corresponds to the directional multipole. The first column shows the results for each model and their Mean Square Error, the second column the Structural Similarity results, and, finally, the third one the Visual Difference Predictor*

Chapter 7

Conclusions

This dissertation evaluates further expansions in the image synthesis of subsurface scattering materials using the diffusion based approximation. It has introduced a new diffusion based model of light transport in thin scattering materials, we've dubbed it the directional multipole because it is a mixture of the dirpole diffusion model and the multipole model. We have shown that this new model achieves a better approximation of the reflectance profile as the distance from the incident point increases. We are not disc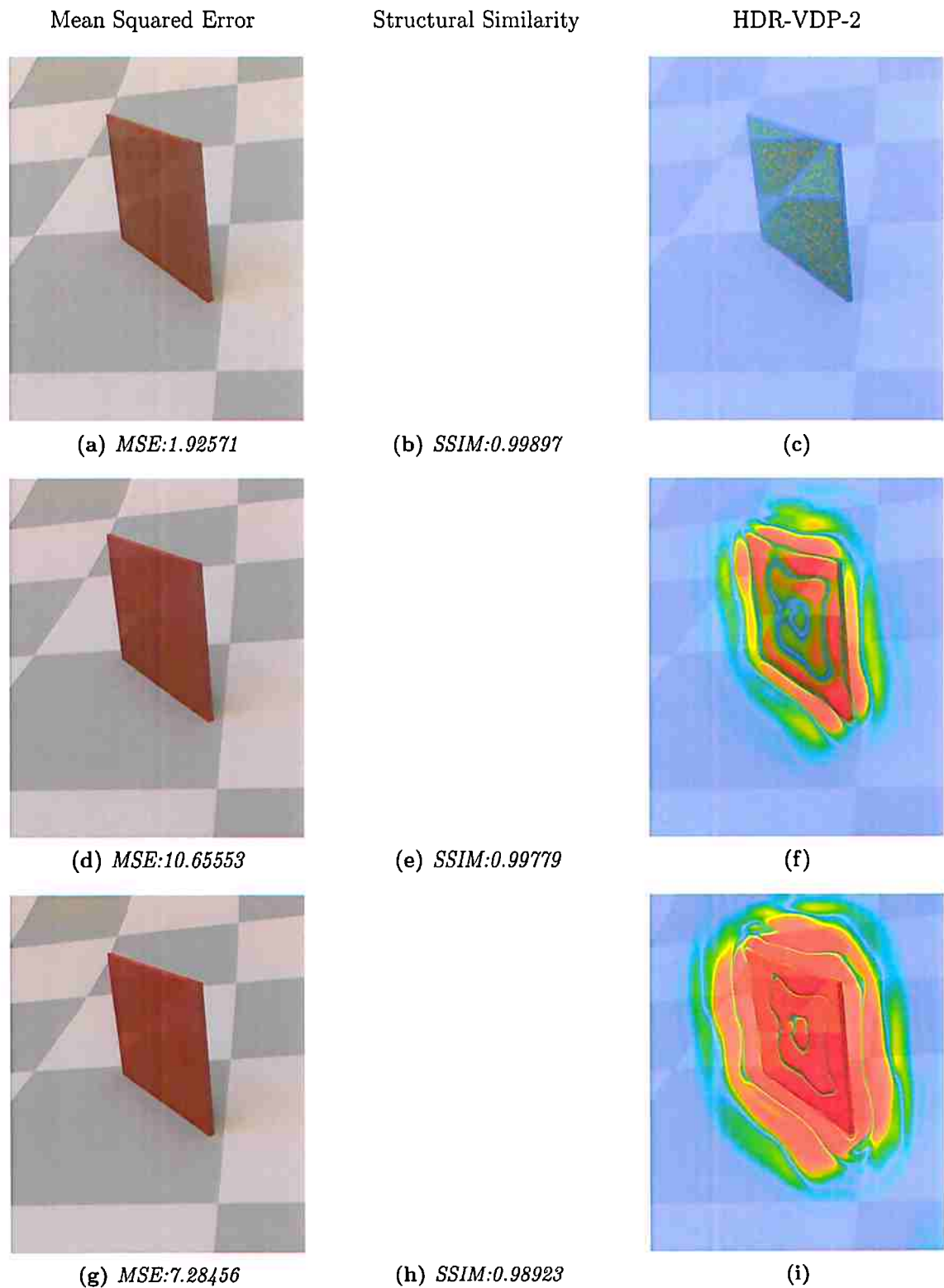ouraged by the overestimation near the incident point because this issue can be fixed using a step function with different *kappa* factors according to the distance to the incident point. We found that this approximation is of most importance in materials with albedo's close to one, where multiple scattering plays an important part in illumination.

We have also given a clear and detailed introduction to diffusion theory and a full derivation of multiple diffusion based models, starting from the dipole model until the directional dipole. This enabled us to analyze the limitations and improvements each of these models brought to the synthesis of translucent materials. Without this we would not have been able to notice where they could be extended and improved upon. Specifically, we found that the directional dipole is limited by its assumptions of semi-infinite geometry, in thin slabs rays may exit at the other surface and therefore this approximation leads the result to an overestimation. Meanwhile the multipole is still a basic representation of the incident light, it represents the diffuse illumination with a point underneath the surface. The directional multipole method brings together the best of the directional dipole and the multipole, which allows the improved representation of translucent material objects with shallow depths. The directional multipole uses the same diffusion solution that the directional dipole does, i.e. the solution for a ray of light, which is a better representation of the rays of light when compared to the point representation used by older models. When we extend this solution to control thin slabs while maintaining the gained accuracy for non-normal incident rays, we obtain a model that is able to provide a better result than those models previously used.

We have compared the results of the directional multipole method with Monte Carlo simulations using parameters previously published as examples of its performance, and have obtained uplifting results. Our model presents the best fit analytically. We have also given several examples of rendered images to improve the visualization of the reflectance profile.

As we showed in Chapter 4, the diffusion approximation based models have evolved in order to provide more accurate solutions to the representation of translucent materials. We combined the best qualities of two of these methods in Chapter 5, but there are still limitations that the new directional multipole method cannot overcome.

Just like the multipole model, there is a restriction on the minimum thickness of the slab, it should be at least two mean free paths thick because the positive source of the 0th order dipole pair must be contained within it. The restriction due to the assumption of high albedo is also present in our model. This restriction is present in all diffusion based models since it is intrinsic to the approximation. However, in the cases where a low albedo is present, single scattering predominates and an approximation ignoring multiple scattering can be more than enough.

The most obvious solution to overcome these limitations is the real path tracing of the interactions beneath the surface. Currently, the improvements in GPU and CPU make this approach a possible option. However, in some environments like the gaming industry it might be an overkill to perform such an expensive computation. This is why creating even better approximations is still a valid and important research.

It would also be interesting to explore whether we can create a deep learning model that is able to predict with increased accuracy and efficiency the diffuse radiance profile. In recent years a lot of complex functions have been approximated using deep learning models. It might be interesting to test whether the Radiance Transfer Equation can be solved using this approach. Though diffusion theory is a great approximation it might be possible that it has reached its limit for translucent material representation.

Appendix A

Appendix

A.1 Hemispherical integrals of the Fresnel reflectance

$$
2C_1 \approx \begin{cases} 0.919317 - 3.4793\eta + 6.75335\eta^2 - 7.80989\eta^3 + \\ \qquad\qquad 4.98554\eta^4 - 1.36881\eta^5 \end{cases}, \quad \eta < 1 \\ \begin{cases} -9.23372 + 22.2272\eta - 20.9292\eta^2 + 10.2291\eta^3 - \\ \qquad\qquad 2.54396\eta^4 + 0.254913\eta^5 \end{cases}, \quad \eta \geq 1 \tag{A.1}
$$

$$
3C_2 \approx \begin{cases} 0.828421 - 2.62051\eta + 3.36231\eta^2 - 1.95284\eta^3 + \\ \qquad\qquad 0.236494\eta^4 + 0.145787\eta^5 \end{cases}, \quad \eta < 1 \\ \begin{cases} -1641.1 + \frac{135.926}{\eta^3} - \frac{656.175}{\eta^2} + \frac{1376.53}{\eta} + 1213.67\eta - \\ \quad 568.556\eta^2 + 164.798\eta^3 - 27.0181\eta^4 + 1.91826\eta^5 \end{cases}, \quad \eta \geq 1 \tag{A.2}
$$

A.2 Importance sampling techniques

- Exponential Sampling. An exponentially decreasing sampling with a PDF proportional to the source term $Q(t)$. Generally used in path tracing, photon mapping, and photon diffusion for choosing propagation distances in homogeneous media.

$$
t_i = \frac{\log(1 - \xi_i)}{\sigma_t'} \quad \text{with} \quad \text{pdf}_{\text{exp}}(t_i) = \sigma_t' e^{-\sigma_t' t_i} \tag{A.3}
$$

where $\xi_i \in [0, 1)$ is a uniform random number. This PDF only depends on t. This means the dipole sources are placed at different depths and are weighted according to the inverse exponential PDF, canceling out the exponential variation in $Q(t)$.

- Equiangular Sampling. At each p, it distributes the samples uniformly in the angular domain subtended by the incident beam. This method was proposed by Kulla and Fajardo [KF12].

$$
t_i = -h \tan\theta_i \quad \text{with} \quad \text{pdf}_{\text{equ}}(t_i | p, \omega) = \frac{h}{(\theta_b - \theta_a)(h^2 + t_i^2)} \tag{A.4}
$$

where h is the distance between p and the beam ω, θ_a and θ_b are the start and end angles of the integration in the angular domain, and $\theta_i = \text{lerp}(\theta_a, \theta_b, \xi_i)$.

Multiple importance sampling (MIS) [VG95] is employed since there are two sampling strategies that perform well in different situations. The exponential sampling represents well the tail of the profile with as little as 1 sample; while the equiangular sampling represents the peak well even with just 1 sample. Since the region for which each strategy works better (tail vs. peak) is known, a

modified MIS weighting heuristic is tailored:

$$R_d \approx \frac{1}{N} \sum_{i=1}^{N} \frac{f(p, \omega, t_i) w_{\text{exp}}(t_i, p)}{w_{\text{exp}}(t_i, p) \text{pdf}_{\text{exp}}(t_i) + w_{\text{exp}}(t_i, p) \text{pdf}_{\text{equ}}(t_i | p, \omega)}$$
$$+ \frac{1}{N} \sum_{j=1}^{N} \frac{f(p, \omega, t_j) w_{\text{equ}}(t_j, p)}{w_{\text{exp}}(t_j, p) \text{pdf}_{\text{exp}}(t_j) + w_{\text{exp}}(t_j, p) \text{pdf}_{\text{equ}}(t_j | p, \omega)} \tag{A.5}$$

where $w_{\text{exp}}(t_i, p) = clamp((p - a)/(b - a), 0, 1)$ and $w_{\text{equ}}(t_i, p) = 1 - w_{\text{exp}}(t_i, p)$. The weighting strategy dedicates samples entirely to the superior PDF except in a small transition zone ($p \in [a, b]$) where it smoothly weights the two strategies. The transition zone is centered around one diffuse mean free path, with $a = 0.9/\sigma_t'$ and $b = 1.1/\sigma_t'$.

Bibliography

[Cli] Cliparts.co. Camera small clipart 300pixel size, free design. 9

[Dav58] B. Davison. *Neutron transport theory*. International series of monographs on physics. Clarendon Press, 1958. 26

[DFG97] Contini D., Martelli F. and Zaccanti G. Photon migration through a turbid slab described by a model based on diffusion approximation. i. theory. *Appl. Opt.*, 36(19):4587–4599, Jul 1997. 23, 31

[dI11] E. d'Eon and G. Irving. A quantized-diffusion model for rendering translucent materials. Em *ACM SIGGRAPH 2011 Papers*, SIGGRAPH '11, páginas 56:1–56:14, New York, NY, USA, 2011. ACM. 16, 22

[DJ05] C. Donner and H. Jensen. Light diffusion in multi-layered translucent materials. Em *ACM SIGGRAPH 2005 Papers*, SIGGRAPH '05, páginas 1032–1039, New York, NY, USA, 2005. ACM. 3, 21, 24

[DJ08] C. Donner and H. Jensen. Rendering translucent materials using photon diffusion. Em *ACM SIGGRAPH 2008 Classes*, SIGGRAPH '08, páginas 4:1–4:9, New York, NY, USA, 2008. ACM. 22

[DL76] J. Duderstadt and Hamilton L. *Nuclear Reactor Analysis*. Wiley, 1976. 13

[Don06] C. Donner. *Towards Realistic Image Synthesis of Scattering Materials*. Tese de Doutorado, University of California at San Diego, La Jolla, CA, USA, 2006. AAI3226771. 13, 15, 18, 19, 23, 31

[FHK14] J. Frisvad, T. Hachisuka and T. Kjeldsen. Directional dipole model for subsurface scattering. *ACM Trans. Graph.*, 34(1):5:1–5:12, December 2014. 3, 22, 25, 27, 28, 30

[Fic55] A. Fick. On liquid diffusion. *The London, Edinburgh, and Dublin Philosophical Magazine and Journal of Science X*, páginas 30–39, 1855. 15

[FPB92] T. Farrell, M. Patterson and Wilson B. A diffusion theory model of spatially resolved, steady-state diffuse reflections for the noninvasive determination of tissue optical properties in vivo. *Med. Phys.*, 19(4):879–888, 1992. 17, 18

[GFTB83] R. Groenhuis, H. Ferwerda and J. Ten Bosch. Scattering and absorption of turbid materials determined from reflection measurements. 1: Theory. *Appl. Opt.*, 22(16):2456–2462, Aug 1983. 16

[GS55] S. Glasstone and A. Sesonske. Nuclear Reactor Engineering. *Van Nostrand Company*, 1955. 2, 13, 16, 17

[HCJ13] R. Habel, P. Christensen and W. Jarosz. Photon beam diffusion: A hybrid monte carlo method for subsurface scattering. Em *Proceedings of the Eurographics Symposium on Rendering*, EGSR '13, páginas 27–37, Aire-la-Ville, Switzerland, Switzerland, 2013. Eurographics Association. 22, 25

[HK93]   P. Hanrahan and W. Krueger. Reflection from layered surfaces due to subsurface scattering. Em *Proceedings of the 20th Annual Conference on Computer Graphics and Interactive Techniques*, SIGGRAPH '93, páginas 165–174, New York, NY, USA, 1993. ACM. 13, 25

[INN07]   T. Igarashi, K. Nishino and S. Nayar. The appearance of human skin: A survey. *Found. Trends. Comput. Graph. Vis.*, 3(1):1–95, January 2007. 2, 3, 4

[Ish78]   A. Ishimaru. *Wave Propagation and Scattering in Random Media.* Academic Press, New York, 1978. 15

[Jen01]   Henrik Wann Jensen. *Realistic Image Synthesis Using Photon Mapping.* A. K. Peters, Ltd., Natick, MA, USA, 2001. 7, 8, 9, 11

[JMLH01] H. Jensen, S. Marschner, M. Levoy and P. Hanrahan. A practical model for subsurface light transport. Em *Proceedings of the 28th Annual Conference on Computer Graphics and Interactive Techniques*, SIGGRAPH '01, páginas 511–518, New York, NY, USA, 2001. ACM. 2, 13, 14, 15, 16, 21, 24, 25, 33

[JWW76]   J. Joseph, W. Wiscombe and J. Weinman. The Delta-Eddington Approximation for Radiative Flux Transfer. *Journal of the Atmospheric Sciences*, 33(12):2452–2459, Dec 1976. 25

[KF12]   C. Kulla and M. Fajardo. Importance sampling techniques for path tracing in participating media. *Comput. Graph. Forum*, 31(4):1519–1528, June 2012. 53

[KP97]   A. Kienle and M. S. Patterson. Improved solutions of the steady-state and the time-resolved diffusion equations for reflectance from a semi-infinite turbid medium. *J. Opt. Soc. Am. A*, 14(1):246–254, Jan 1997. 25

[Lam60]   J. Lambert. *Photometria sive De mensura et gradibus luminis, colorum et umbrae.* Sumptibus viduae Eberhardi Klett, typis Christophori Petri Detleffsen, 1760. 9

[LL07]   Wang L. and Jacques S. L. (mcml) monte carlo for multi-layered media, 2007. 33

[MSG05a] S. Menon, Q. Su and R. Grobe. Determination of g and μ using multiply scattered light in turbid media. *Physical Review Letters*, 94, Apr 2005. 25

[MSG05b] S. Menon, Q. Su and R. Grobe. Generalized diffusion solution for light scattering from anisotropic sources. *Optics Letters*, 30(12):1542–1544, Jun 2005. 3, 22, 25

[NGD+06] S. Narasimhan, M. Gupta, C. Donner, R. Ramamoorthi, S. Nayar and H. Jensen. Acquiring scattering properties of participating media by dilution. Em *ACM SIGGRAPH 2006 Papers*, SIGGRAPH '06, páginas 1003–1012, New York, NY, USA, 2006. ACM. 33

[PH10]   M. Pharr and G. Humphreys. *Physically Based Rendering, Second Edition: From Theory To Implementation.* Morgan Kaufmann Publishers Inc., San Francisco, CA, USA, 2nd edição, 2010. 1, 8, 9, 10, 11, 12, 13, 14

[Pla08]   Placbo. Milk Splash, 2008. 1

[PSW89]   M. Patterson, E. Schwartz and B. Wilson. Quantitative reflectance spectrophotometry for the noninvasive measurement of photosensitizer concentration in tissue during photodynamic therapy. Em *Proc. SPIE*, volume 1065, páginas 115–122, 1989. 18

[Ray71]   J. Rayleigh. On the scattering of light by small particles. *Philosophical magazine*, 61:447–454, 1871. 2

[Rei73]   J. Reichman. Determination of Absorption and Scattering Coefficients for Nonhomogeneous Media. 1: Theory. *Appl. Opt.*, 12(8):1811–1815, Aug 1973. 17

[RRBG06]   J. Ramella-Roman, B. Boulbry and T. Germer. Models, 2006. 3

[Rus06]   K. Rush. Cleopatra Statue, 2006. 1

[ToPoIE07]   V. Tuchin and Society of Photo-optical Instrumentation Engineers. *Tissue Optics: Light Scattering Methods and Instruments for Medical Diagnosis*. Press Monographs. SPIE/International Society for Optical Engineering, 2007. 24

[VG95]   E. Veach and L. Guibas. Optimally combining sampling techniques for monte carlo rendering. Em *Proceedings of the 22Nd Annual Conference on Computer Graphics and Interactive Techniques*, SIGGRAPH '95, páginas 419–428, New York, NY, USA, 1995. ACM. 53

[VGJSS89]   M. Van Gemert, S. Jacques, H. Sterenborg and W. Star. Skin optics. *Biomedical Engineering, IEEE Transactions on*, 36(12):1146–1154, Dec 1989. 14

[Wan98]   L. Wang. Rapid modeling of diffuse reflectance of light in turbid slabs. *J. Opt. Soc. Am. A*, 15(4):936–944, Apr 1998. 23, 31